Draft version March 28, 2023
Typeset using LaTeX **twocolumn** style in AASTeX631

arXiv:2303.14571v1 [astro-ph.EP] 25 Mar 2023

Fishing for Planets: A Comparative Analysis of EPRV Survey Performance in the Presence of Correlated Noise

Arvind F. Gupta [1,2] and Megan Bedell [3]

[1] Department of Astronomy & Astrophysics, 525 Davey Laboratory, The Pennsylvania State University, University Park, PA, 16802, USA
[2] Center for Exoplanets and Habitable Worlds, 525 Davey Laboratory, The Pennsylvania State University, University Park, PA, 16802, USA
[3] Center for Computational Astrophysics, Flatiron Institute, 162 5th Avenue, New York, NY 10010, USA

Submitted to AJ

ABSTRACT

With dedicated exoplanet surveys underway for multiple extreme precision radial velocity (EPRV) instruments, the near-future prospects of RV exoplanet science are promising. These surveys' generous time allocations are expected to facilitate the discovery of Earth analogs around bright, nearby Sun-like stars. But survey success will depend critically on the choice of observing strategy, which will determine the survey's ability to mitigate known sources of noise and extract low-amplitude exoplanet signals. Here, we present an analysis of the Fisher information content of simulated EPRV surveys, accounting for the most recent advances in our understanding of stellar variability on both short and long timescales (i.e., oscillations and granulation within individual nights, and activity-induced variations across multiple nights). In this analysis, we capture the correlated nature of stellar variability by parameterizing these signals with Gaussian Process kernels. We describe the underlying simulation framework as well as the physical interpretation of the Fisher information content, and we evaluate the efficacy of EPRV survey strategies that have been presented in the literature. We explore and compare strategies for scheduling observations over various timescales and we make recommendations to optimize survey performance for the detection of Earth-like exoplanets.

Keywords: Exoplanet Detection Methods – Radial Velocity – Surveys – Fisher Information – Stellar Activity

1. INTRODUCTION

For several decades, astronomers have been carrying out systematic radial velocity (RV) surveys to search for exoplanets around nearby stars. The first detection of an exoplanet orbiting a main sequence star by Mayor & Queloz (1995) was the result of one such search, and this discovery spurred decades of interest and accelerating progress in exoplanet science. As instrumentation and analysis techniques have improved, as evidenced by the growing class of spectrographs capable measuring Doppler signals with sub-m s^{-1} precision, so too have the prospects of exoplanet surveys.

Corresponding author: Arvind F. Gupta
arvind@psu.edu

Several of these extreme precision radial velocity (EPRV) spectrographs support exoplanet surveys with generous time allocations, totalling hundreds to thousands of hours each year for up to a decade. These include the EXPRES 100 Earths Survey (Jurgenson et al. 2016; Brewer et al. 2020), the NEID Earth Twin Survey (Schwab et al. 2016; Gupta et al. 2021), the upcoming Terra Hunting Experiment (Hall et al. 2018) with HARPS-3 (Thompson et al. 2016), the HARPS-N Rocky Planet Search (Cosentino et al. 2012; Motalebi et al. 2015), and a blind radial velocity survey with ESPRESSO (Pepe et al. 2021; Hojjatpanah et al. 2019). While the exact objectives of each survey vary, two common themes are the discovery and characterization of habitable-zone, Earth-mass exoplanets and the refinement of intrinsic exoplanet occurrence rate statistics, particularly for exoplanets in mass and period regimes

that were inaccessible to previous instruments. At the intersection of these two goals is a robust measurement of the frequency of Earth analog exoplanets, $\eta_\oplus$, a quantity that will drive the design of future direct imaging missions (Crass et al. 2021).

Drawing accurate conclusions about $\eta_\oplus$ and other exoplanet populations from these efforts depends critically on being able to calculate the detection sensitivity limits of RV surveys. Early studies such as Cumming (2004) and Zechmeister et al. (2009) outline methods of computing detection sensitivity limits via periodogram analysis, accounting for observational measurement errors and the expected form of Keplerian signals. This type of approach was implemented in exoplanet yield analyses from programs the Eta Earth survey with HIRES (Howard et al. 2010) and the HARPS and CORALIE planet searches (Mayor et al. 2011), both of which shed light on the occurrence rates of short-period exoplanets with $m \sin i$ limits approaching $1 M_\oplus$. These analytic, periodogram-based prescriptions were sufficient for surveys with instrumental precisions well over 1 m s^{-1}; for relatively quiet stars, stellar variability signals did not contribute significantly to the bulk uncertainty. But with the arrival of EPRV spectrographs capable of delivering instrumental RV precisions at the 1 m s^{-1} and even sub-m s^{-1} levels, detection limits are expected to depend strongly on correlated noise from intrinsic stellar variability. Indeed, intrinsic stellar variability has been identified as the largest remaining hurdle for RV detection of Earth-like exoplanets (Crass et al. 2021), and large-scale survey simulations show that correlated noise will limit sensitivity to Earth-like planets (Newman et al. 2022; Luhn et al. 2023).

When correlated noise sources are expected to be significant, it is common to instead assess detection limits via injection-recovery tests, in which synthetic exoplanet signals are injected into the RV time series for each star and models are used to attempt to fit and recover the exoplanet-induced signal (e.g., Howard & Fulton 2016; Rosenthal et al. 2021; Laliotis et al. 2023). The recovery rate in a given region of parameter space (e.g., at a certain planet mass and orbital period) informs the detection sensitivity of the survey. Because this approach uses not only the measurement uncertainties but also the RV measurements themselves, it fares much better in establishing detection sensitivity limits in the regime in which correlated noise sources dominate, as intrinsic stellar RV signals can be injected alongside exoplanet-induced signals. In addition, the 'recovery' portion of this method highlights the fact that the reported detection limits account not only for the survey itself (i.e., the observed data), but also for the analysis methods applied – these limits are model dependent. This is particularly important to note given the emergence of increasingly sophisticated treatments of stellar RV variability as an astrophysical signal that can be modeled and understood rather than a simple source of noise (e.g., Rajpaul et al. 2015; Gilbertson et al. 2020b; Aigrain & Foreman-Mackey 2022; Haywood et al. 2022).

Injection-recovery tests are particularly effective when analyzing existing data, but they are not an ideal tool for analyzing simulations of future surveys. Yet such simulations will need to become standard practice to ensure the efficient use of EPRV observing resources. For surveys for which design decisions such as cadence, exposure times, or even target lists have yet to be determined, simulating a single survey realization will not suffice. We expect our ability to mitigate the noise contributions from intrinsic stellar variability and extract exoplanet-induced signals will be greatly impacted by the enacted observing scheme (Dumusque et al. 2011; Hall et al. 2018; Chaplin et al. 2019; Luhn et al. 2023), and a sizeable parameter space of survey strategies will need to be explored to test these predictions. In addition, astronomical observations are subject to the stochastic nature of weather conditions and other practical constraints; we cannot precisely predict the observed sampling of the RV time series for a given star even when a desired survey strategy has been finalized. Many sets of observations would need to be simulated and followed up with injection-recovery tests to achieve statistically robust results, further increasing the computational expense. Finally, injection-recovery tests can be poor predictors of survey yields given that the tools with which we identify and characterize exoplanet-induced signals will evolve between the conception and completion of long-term surveys.

In this work, we present a framework in which we use Fisher information analysis to quantify the intrinsic information content of simulated RV observations and to predict the detection limits achieved by ongoing and future EPRV exoplanet surveys in a computationally efficient manner. We show that such a tool can be used not only to translate yields into occurrence rates, but also to identify survey strategies that will optimize sensitivity to specific populations of exoplanets, such as Earth analogs. We describe the Fisher information calculation in Section 2 and the input Gaussian process (GP) kernels with which we parameterize contributions from stellar variability in Section 3. In Section 4, we compare the detection limits achieved by sets of simulated observations across various timescales to formulate an idealized survey design. We apply these findings to full survey simulations in Section 5, in which we also de-

scribe our observation simulation tool that accounts for practical observing constraints to ensure realistic survey realizations. And we discuss our results and their implications in Section 6 and caveats and prospects for future work in Section 7.

2. FISHER INFORMATION

The Fisher information content of a data set can be used to calculate the expected uncertainty on a set of parameters for a representative model (Fisher 1922). For a model with a single independent variable (e.g., a time series), the Fisher information, B, is given as the Hessian of the negative log likelihood function

$$B_{i,j} = -\frac{\partial^2 \ln \mathcal{L}}{\partial\theta_i \partial\theta_j} \tag{1}$$

where θ is the parameter vector and the log likelihood is

$$\begin{aligned} \ln \mathcal{L} = -\frac{1}{2}\big[&(x-\mu)^T C^{-1}(x-\mu) \\ &+ N \ln 2\pi + \ln \det C\big] \end{aligned} \tag{2}$$

for a model μ and time series x of length N, and a $N \times N$ covariance matrix, C, that describes the expected noise properties of the measurements. Both μ and C may depend on θ in the general case.

In the case that the model parameters are independently Gaussianly distributed, the Fisher information can be written as

$$\begin{aligned} B_{i,j} = &\left(\frac{\partial\mu}{\partial\theta_i}\right)^T C^{-1} \left(\frac{\partial\mu}{\partial\theta_j}\right) \\ &+ \frac{1}{2}\mathrm{tr}\left(C^{-1}\frac{\partial C}{\partial\theta_i}C^{-1}\frac{\partial C}{\partial\theta_i}\right) \end{aligned} \tag{3}$$

or if the covariance is independent of the model parameters, simply

$$B_{i,j} = \left(\frac{\partial\mu}{\partial\theta_i}\right)^T C^{-1} \left(\frac{\partial\mu}{\partial\theta_j}\right). \tag{4}$$

The diagonal elements of the inverse of the Fisher information matrix represent the parameter uncertainties:

$$\sigma^2_{\theta_i} = B^{-1}_{i,i}. \tag{5}$$

It is important to note here that the time series x has dropped out of the equation, and the Fisher information depends only on the model μ, the covariance matrix C, and the times t at which measurements are taken. That is, we do not need to know the measured values of x to determine the expected parameter uncertainties.

The use of Fisher information analyses for astronomical data sets was first studied by Tegmark et al. (1997), who explored the utility of this metric in the context of cosmology. More recent applications include the work of Gomes et al. (2022), who assess sensitivity to gravitational effects of an as-yet undetected outer Solar System planet, and that of Cloutier et al. (2018), who introduced Fisher information analysis to RV exoplanet science with applications to follow-up observations of transiting exoplanets and considerations for correlated noise signals. Here, we adopt the notation used in Cloutier et al. (2018) and present a new framework for using Fisher information to calculate detection sensitivity limits for blind RV exoplanet surveys. The RV semi-amplitude induced by a single exoplanet with mass M_p and period P orbiting a star with mass $M_\star$ is

$$K = \frac{M_p \sin i}{\sqrt{1-e^2}} \left(\frac{2\pi G}{(M_\star + M_p)^2 (P)}\right)^{1/3}. \tag{6}$$

For our model in this work, we assume circular, zero-eccentricity orbits and single-planet systems such that the exoplanet-induced RV signal can be represented with a simplified Keplerian

$$\mu(t) = K \sin\left(\frac{2\pi}{P}t - \phi_0\right), \tag{7}$$

where ϕ_0 is an initial phase offset and t is the set of observation times. The corresponding parameter vector is then

$$\theta = \{K, P, \phi_0\}, \tag{8}$$

and the derivative of the model with respect to this vector is

$$\frac{\partial\mu}{\partial\theta} = \begin{bmatrix} \frac{\partial\mu}{\partial K} \\ \frac{\partial\mu}{\partial P} \\ \frac{\partial\mu}{\partial\phi_0} \end{bmatrix} = \begin{bmatrix} \sin(\frac{2\pi}{P}t - \phi_0) \\ -\frac{2\pi t}{P^2} K \cos(\frac{2\pi}{P}t - \phi_0) \\ -K\cos(\frac{2\pi}{P}t - \phi_0) \end{bmatrix}. \tag{9}$$

The inclusion of a covariance matrix in Equation 4 allows us to capture the effect of correlated noise on the achieved RV sensitivity. In a pure white noise scenario, C will be a matrix with elements $C_{n,m} = \sigma_n^2 \delta_{nm}$, where σ_n is the total measurement uncertainty for observation $1 \leq n \leq N$ and δ is the delta function

$$\delta_{nm} = \begin{cases} 1 & m = n \\ 0 & m \neq n \end{cases}. \tag{10}$$

That is, all the off-diagonal elements will be 0; independent measurements will have independent noise properties. But if correlated noise sources are present, some off-diagonal elements will be non-zero as well, representing covariances between the noise properties of pairs of observations. We discuss anticipated sources of noise and the construction of a covariance matrix for EPRV data sets in the following section.

3. CONSTRUCTING A COVARIANCE MATRIX FOR RADIAL VELOCITY OBSERVATIONS

The full covariance matrix to be used in Equation 4 will be made up of a sum of white noise and correlated noise components

$$C = \sigma^2_{\rm photon} I + k_{\rm osc} + k_{\rm gran} + k_{\rm activity}, \tag{11}$$

where I is the $N \times N$ identity matrix and the remaining terms are described below.

The primary source of white noise is photon noise, or the limit on the precision of an individual RV measurement as determined by the Doppler information content of the observed stellar spectrum. The photon noise limit, $\sigma_{\rm photon}$, depends on the wavelength range and spectral features from which the RV measurement is derived and on the observed signal-to-noise ratio (S/N) across this spectral range, and it can be calculated analytically as shown by Bouchy et al. (2001).

Instrument systematics and RV variations due to intrinsic stellar variability constitute two important sources of correlated noise that will impact RV exoplanet discovery efforts (Crass et al. 2021). In this work, we will focus primarily on the correlated nature of stellar variability. Well-characterized instrument systematics are typically modeled and calibrated out during the data reduction process for EPRV spectrographs (e.g., Halverson et al. 2016; Petersburg et al. 2020). These signals are largely absent from the resulting RV time series, and correlations in any $\ll 1$ m s^{-1} level residuals will be poorly understood and difficult to model. Here, we consider the post-calibration RV time series as our starting point, such that any systematics that can be removed have been removed, and we will reserve a more detailed discussion of instrument-related correlated noise for Section 7.2.

Intrinsic stellar RV variations are present in the final RV time series at the ~ 1 m s^{-1} level for typical observations of quiet exoplanet search targets. To account for these stellar signals, it is common practice to model them using Gaussian process (GP) regression while simultaneously fitting for an exoplanet-induced signal (see review by Aigrain & Foreman-Mackey 2022). This approach provides for straightforward integration with the covariance matrix, as one can build individual sources of variability into this matrix with appropriate GP kernel functions. In the remainder of this section, we describe the dominant sources of stellar variability for typical Sun-like G- and K-dwarfs and we present the form of their respective GP kernels.

On short timescales, i.e., less than a single night, the most important sources of stellar RV variations are p-mode oscillations, which manifest as m s^{-1}-level variations on 5-10 minute timescales, and surface granulation, which has a similar amplitude on slightly longer timescales. For oscillations, we adopt the GP kernel described by Luhn et al. (2023) and based on work by Pereira et al. (2019) and Guo et al. (2022), which takes the form

$$\begin{aligned} k_{\rm osc}(\Delta) = S_{\rm osc}\omega_{\rm osc} Q e^{\frac{-\omega_{\rm osc}\Delta}{2Q}} \\ \times \left(\cos(\eta\omega_{\rm osc}\Delta) + \frac{1}{2\eta Q}\sin(\eta\omega_{\rm osc}\Delta)\right), \end{aligned} \tag{12}$$

where Δ is the $N \times N$ matrix that represents the absolute value of the time delay between pairs of observations

$$\Delta_{n,m} = |t_n - t_m|. \tag{13}$$

$S_{\rm osc}$ is the power at the peak of the oscillation excess, $\omega_{\rm osc}$ is the characteristic oscillation frequency, Q is the quality factor, and $\eta = |1 - (4Q^2)^{-1}|^{1/2}$.

We also adopt the following two-component granulation kernel from Luhn et al. (2023) and Guo et al. (2022):

$$\begin{aligned} k_{\rm gran}(\Delta) = S_1\omega_1 e^{\frac{-\omega_1\Delta}{\sqrt{2}}}\cos\left(\frac{\omega_1\Delta}{\sqrt{2}} - \frac{\pi}{4}\right) \\ + S_2\omega_2 e^{\frac{-\omega_2\Delta}{\sqrt{2}}}\cos\left(\frac{\omega_2\Delta}{\sqrt{2}} - \frac{\pi}{4}\right), \end{aligned} \tag{14}$$

where S_1 and S_2 describe the power of each granulation component and ω_1 and ω_2 are the respective characteristic frequencies. We show the form of the oscillation and granulation kernels in Figure 1, assuming perfectly Solar hyperparameters as given in Table 1.

Stellar RV variability resulting from rotational modulation of active regions and starspots is our primary source of correlated noise on longer timescales. Activity-induced variability is commonly modeled using a quasi-periodic GP kernel of the form

$$k_{{\rm activity},QP}(\Delta) = \alpha^2 \exp\left(-\frac{\Delta^2}{2\lambda_1^2} - \Gamma\sin^2\left(\frac{\pi\Delta}{\lambda_2}\right)\right) \tag{15}$$

where α is the RV amplitude, λ_1 is the coherence timescale, λ_2 represents the stellar rotation period, and Γ is the periodic complexity factor, or in this case, the complexity of the spot and active region coverage across the stellar surface. This kernel has been shown to be effective for disentangling exoplanet- and activity-induced RV signals, and each hyperparameter has a clear physical interpretation, making it a natural choice for modeling RV time series data in the presence of activity. However, recent work by Gilbertson et al. (2020b) based on simulated solar spectra (Gilbertson et al. 2020a) has

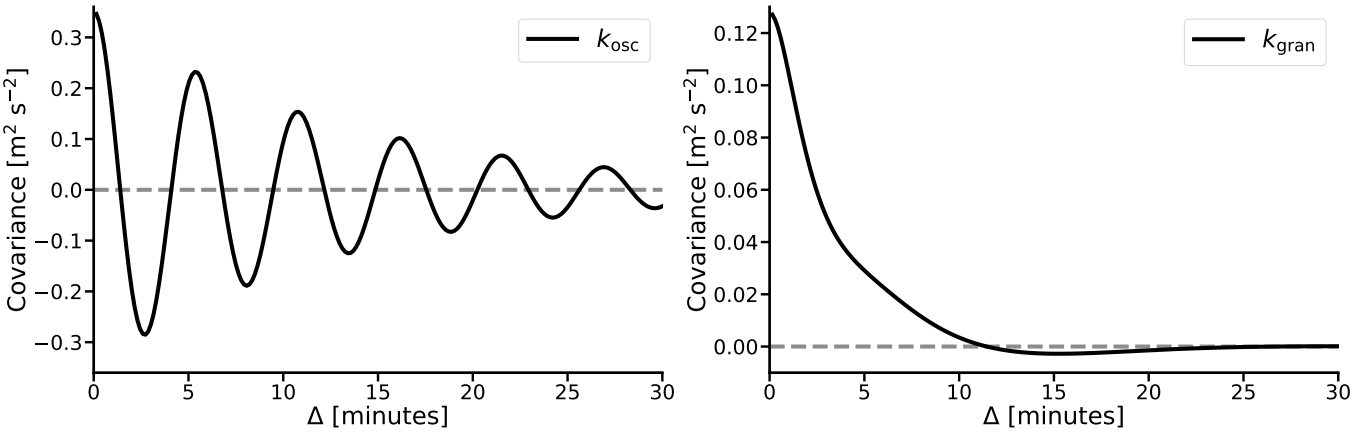


Figure 1. Covariance between pairs of observations as a function of separation in time for the GP kernels for stellar oscillations (Equation 12; left) and for stellar surface granulation (Equation 14; right). We assume instantaneous exposures for both kernels. We show that oscillations and granulation only introduce significant RV noise on short timescales of less than a single night.

Table 1. Solar Hyperparameter Values for Stellar Variability Gaussian Process Kernels

Kernel	Parameter	Value	Units
[a] $k_{\rm osc}$	$S_{\rm osc}$	2.36	m^2 rad^{-1} s^{-1}
	$\omega_{\rm osc}$	0.0195	rad s^{-1}
	Q	7.63	
[a] $k_{\rm gran}$	S_1	18.64	m^2 rad^{-1} s^{-1}
	S_2	5.22	m^2 rad $^{-1}$ s^{-1}
	ω_1	0.00485	rad s^{-1}
	ω_2	0.0173	rad s^{-1}
[b] $k_{{\rm activity},QP}$	α	1.44	m s^{-1}
	Γ	1.486	
	λ_1	23.6	days
	λ_2	28.1	days
[c] $k_{{\rm activity},M\,52}$	a_0	−0.106884	m s^{-1}
	a_1	−1.154	m s^{-1}
	λ	2.52	days

[a] Parameters calculated following the precsription of Luhn et al. (2023) for $T_{\rm eff} = 5777$ K, $\log g = 4.43$, $\nu_{\rm max} = 3100$ μHz

[b] Parameters derived by Langellier et al. (2021) via fit to HARPS-N solar data

[c] Parameters given by Luhn et al. (2023), derived from Gilbertson et al. (2020b) spot-induced solar RV variability simulations

shown other kernels outperform the quasi-periodic kernel, particularly for detecting exoplanets with $K \leq 30$ cm s^{-1}. We therefore also consider the following latent GP kernel

$$k_{{\rm activity},M\,52}(\Delta) = a_0^2 k_{M\,52}(\Delta) - a_1^2 \frac{d^2}{dt^2} k_{M\,52}(\Delta) \quad (16)$$

which is a linear combination of the Matern-5/2 kernel

$$k_{M\,52}(\Delta) = e^{-\frac{\sqrt{5}\Delta}{\lambda}} \left(1 + \frac{\sqrt{5}\Delta}{\lambda} + \frac{5\Delta^2}{3\lambda^2}\right) \quad (17)$$

and its second derivative, with a single timescale hyperparameter, λ, and amplitude coefficients a_0 and a_1. We refer the reader to Gilbertson et al. (2020b) and Luhn et al. (2023) for the calculation of the second derivative of the Matern-5/2 kernel and for a full derivation of Equation 16. We show both activity kernels in Figure 2. For the Matern-5/2 kernel, we assume hyperparameters as derived by Gilbertson et al. (2020b) and for the quasiperiodic kernel, we assume hyperparameters from a fit to HARPS-N solar data by (Langellier et al. 2021). Both sets of hyperparameters are given in Table 1. In subsequent sections, we test survey performance using each of the two activity kernels and comment on how our conclusions change based on the assumed kernel form.

4. FORMULATING AN IDEALIZED SURVEY STRATEGY

We begin our investigation of survey performance with a set of experiments intended to isolate each source of correlated noise and identify observing strategies that will best mitigate their respective impacts on exoplanet detection sensitivity. Separate sets of simulated observing schedules are generated to highlight the effects of stellar RV signals that vary on timescales of less than a single night for Sun-like stars, granulation and p-mode oscillations, and those that span multiple nights, namely active regions and spots. For each set of observations, we calculate the resulting Fisher information and assess the achieved sensitivity limits. In all cases, we assume perfectly Solar hyperparameters for the GP kernels with which we build each covariance matrix.

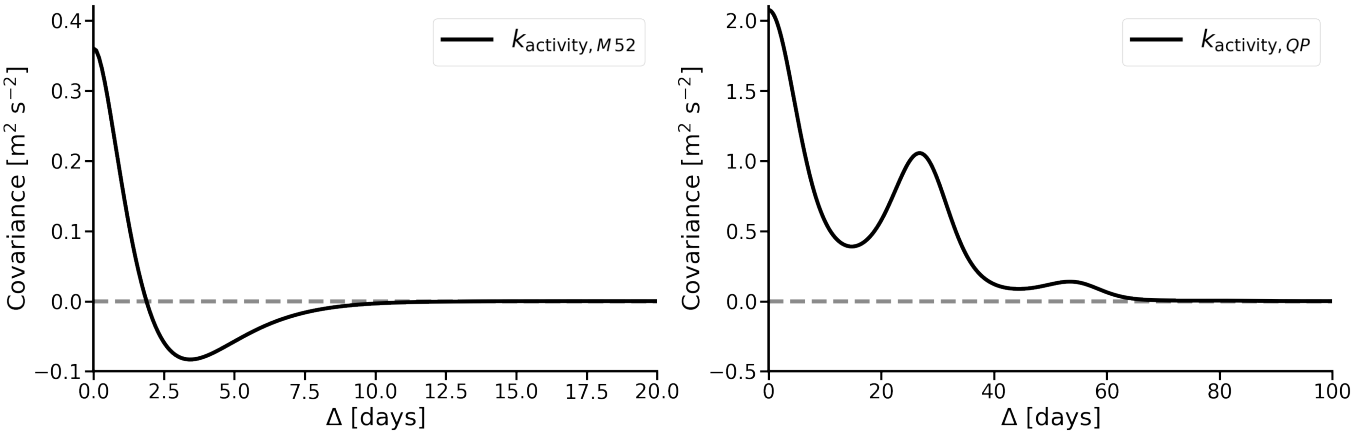


Figure 2. Covariance between pairs of observations as a function of separation in time for the quasiperiodic kernel for rotationally-modulated stellar activity (Equation 15; left) and for the Matern-5/2 kernel for rotationally-modulated stellar activity (Equation 16; right). While the covariance for both kernels persists across many nights, we note that the curves differ significantly in amplitude and shape.

4.1. *Intra-night Observing Schedule Simulations*

As we show in Figure 1, correlations in oscillation and granulation RV signals are not expected to remain coherent for longer than an hour for Sun-like stars, so observations collected on separate nights are effectively independent. To assess the impact of oscillations and granulation on detection sensitivity limits, we therefore explore different strategies for distributing observations within a single night. We consider the following intra-night cadences:

- six visits with one exposure per visit,
- three visits with two exposures per visit,
- two visits with three exposures per visit,
- one visit with six exposures,
- and one visit with a single continuous exposure.

For each of these cadences, we generate 100 nights of observation times across a 500-night baseline (average inter-night separation of 5 nights), and we repeat this for exposure times 15 s $\leq t_{\text{exp}} \leq$ 1200 s. For the three strategies with multiple visits, the start times of each visit are evenly distributed across a six hour window. For the three strategies with multiple exposures in a single visit, the exposures are separated by a readout time, t_r. We then calculate the Fisher information of the simulated observations for covariance matrices consisting of correlated noise from (i) p-mode oscillations, (ii) granulation, (iii) p-mode oscillations and granulation, and (iv) p-mode oscillations, granulation, and photon noise. We do not include an instrumental jitter term for these tests, as we are interested only in the impact of short timescale correlations.

For oscillations and granulation, we start with the GP kernels in Equations 12 and 14. However, as Luhn et al. (2023) note, exposures are not instantaneous, and the exposure times we consider here are comparable to the variability timescales for oscillations and granulation in the case of Sun-like stars. We therefore compute the double integral of these GP kernels over the exposure times to calculate the true covariance between pairs of observations. A detailed discussion of the oscillation and granulation kernel integration is given in the Appendix of Luhn et al. (2023). The assumed hyperparameters are given in Table 1. We determine the photon noise using the NEID exposure time calculator, described in Gupta et al. (2021), for Solar analogs with $V = 4$ and 8 mag.

Finally, we use the covariance matrices and simulated observation times to evaluate the performance of each strategy, where the performance is defined as the expected uncertainty on the semi-amplitude, σ_K, using Equations 4 and 5. We calculate this value for an exoplanet with orbital parameters $K = 10$ cm s^{-1} and $P = 100$ d, marginalizing over phases uniformly distributed on the interval $0 \leq \phi_0 < 2\pi$. The dependence of σ_K on the total nightly time cost of each strategy is shown in Figure 3, where the time cost is calculated as the sum of the exposure times and associated overheads, i.e., readout and target acquisition time (t_{acq}):

$$t_{\text{night}} = N_{\text{visits}}(t_{\text{acq}} + N_{\text{exp}} t_{\text{exp}} + (N_{\text{exp}} - 1)t_r). \quad (18)$$

We assume here that the target need only be acquired once per visit and that the readout cost of the final exposure in a sequence can folded into the cost of acquiring the subsequent target. We use overhead costs of 30 seconds and 180 seconds for readout and acquisition, re-

spectively, to match typical overheads for observations of bright stars with the NEID spectrograph.

4.2. *Intra-night Observing Strategy Results*

In Figure 3, we show that in the presence of correlated noise from oscillations alone, the expected semi-amplitude uncertainty, σ_K, falls off much more rapidly for the single-visit strategies than for the multi-visit strategies across all nightly time allocations. These strategies take advantage of the significant negative covariance seen on timescales comparable to $1/\nu_{\rm max}$, rapidly averaging out the p-mode signal rather than allowing it to bin down like white noise when the covariance approaches zero (i.e., when exposures are widely separated relative to the oscillation periods for Sun-like stars). But it is interesting that neither σ_K nor the relative performance of the different intra-night strategies changes monotonically with nightly time cost. Instead, each intra-night strategy produces several local minima and maxima in σ_K, and these features emerge at different values of $t_{\rm night}$. For granulation, on the other hand, while σ_K does decrease monotonically, the relative performance of each observing strategy is inverted. This can be attributed to the positive covariance of the granulation signal, which is not conveniently averaged out on short timescales. In contrast to oscillations, the correlated noise contribution from granulation is optimally minimized by taking exposures separated by $\Delta \gtrsim 15$ minutes, where the covariance asymptotically approaches zero. However, our results for the combined case with both oscillations and granulation do not consistently prefer the six-visit strategy. Instead, every strategy yields the lowest value of σ_K for at least one value of $t_{\rm night}$ when we include both covariance kernels. That is, the relative advantages of a single-visit strategy, which is optimal for averaging out the oscillation signal, and a multi-visit strategy, which is optimal for binning down the granulation signal, will win out on different time scales. It is also important to note that the optimal strategy for any given nightly time cost will depend on the oscillation and granulation kernel hyperparameter of the specific star being observed. Here, we have assumed perfectly Solar hyperparameters, but these values will vary from star to star.

These results are largely consistent with those of previous studies that explore the RV noise contributions from oscillations and granulation. Chaplin et al. (2019) recently presented a model for predicting residual p-mode oscillation amplitudes as a function of exposure time and stellar parameters, showing that local minima in the residual amplitude curve are present for exposure times close to integer multiples of $\nu_{\rm max}$, the central frequency of the oscillation power excess. This model has since become widely used in the design of EPRV observations, both for exoplanet surveys (e.g., Brewer et al. 2020; Gupta et al. 2021) as well as for studies of stellar signals (e.g., Sulis et al. 2022; Gupta et al. 2022). The covariance behavior of the oscillation kernel we use here (Equation 12) produces these same local minima, albeit on different timescales due to our inclusion of overheads costs and noncontiguous observations. But while the Chaplin et al. (2019) model suggests that the best strategy is one that averages over the oscillations, our results demonstrate the relative advantage of sampling the oscillation signal instead. In the Fisher information framework, the strategy with six consecutive exposures outperforms the continuous exposure strategy on short timescales, because this sampling allows us to use the measured RVs and known GP kernel form to model out the oscillation signal.

We also compare our findings to those of Dumusque et al. (2011), who simulate measurements of stellar RV signals from fitted asteroseismic power spectra, including both oscillations and granulation, and calculate the predicted RV rms for several years of simulated data with different intra-night exposure times and cadences. For the Sun-like, G2V star α Cen A, Dumusque et al. (2011) find that they can achieve a lower RV rms by distributing observations across many hours instead of concentrating them in a single visit with the same total on-sky exposure time. We see the same trend for the granulation-only case in Figure 3, in which the six-visit strategy outperforms the other strategies by a significant margin for nightly time costs up to one hour, but not with oscillations and granulation together.

While the difference between our results and those of the Dumusque et al. (2011) simulations can be partly attributed to our method for calculating the expected RV uncertainty, i.e., Fisher information analysis vs. synthesizing RVs from a power spectrum, some other differences in our approach should be noted. First, Dumusque et al. (2011) do not account for overheads when comparing the performances of different observing cadences. Cadences with more visits are not penalized for the additional overhead costs that will be incurred, so their performance relative to cadences with fewer visits is exaggerated. On the other hand, their study includes the effects of supergranulation and a constant instrument noise floor, both of which introduce correlated noise on timescales longer than oscillations and granulation alone. Because we neglect these sources of correlated noise, we diminish the relative benefits of increasing the spacing between observations. We comment

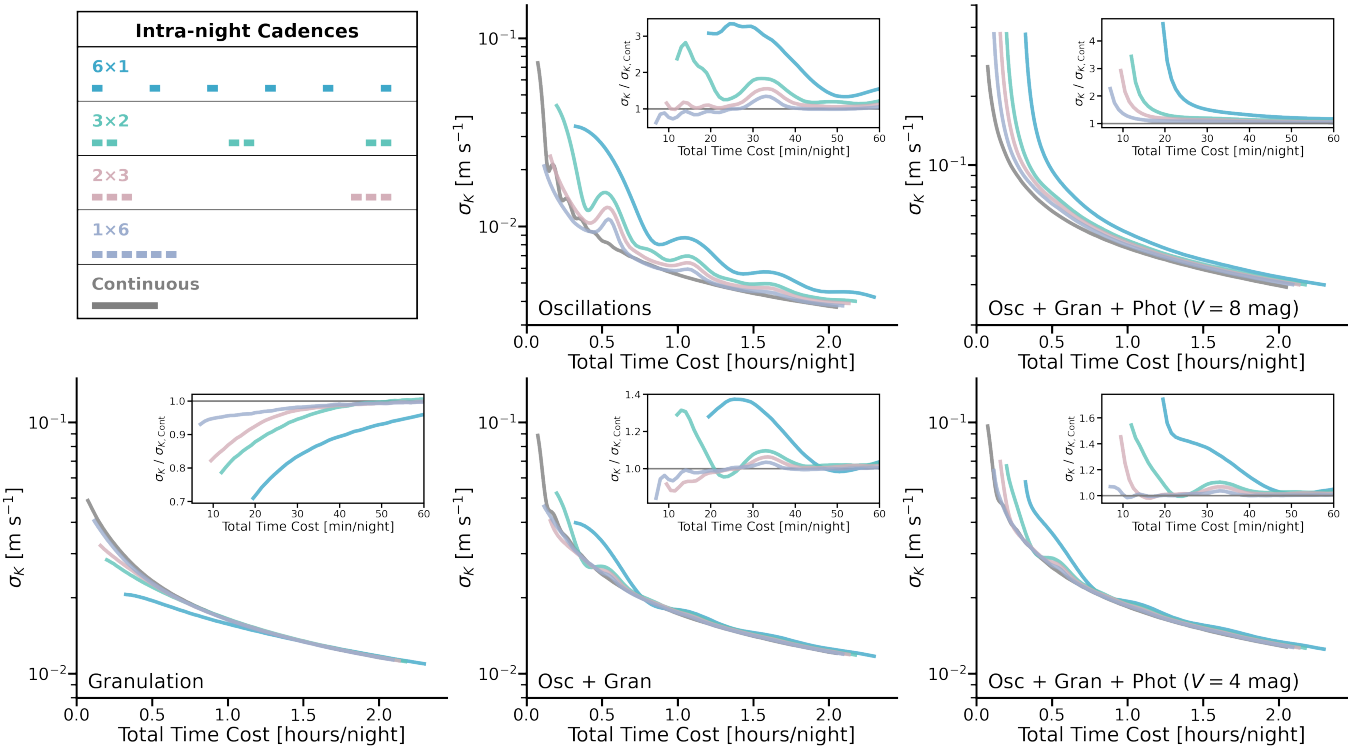


Figure 3. Expected semi-amplitude uncertainty, σ_K, for a $K = 10$ cm s^{-1} signal and an orbital period of $P = 100$ days as a function of total nightly time cost (as calculated via Equation 18). We calculate σ_K for simulated observing schedules with 100 nights of observations distributed across 500 total nights, wherein the observations on each night are distributed according to each of the five strategies depicted in the upper left panel. These strategies are described in Section 4.1. In the remaining panels, we show the impact of contributions from various combinations of photon noise and correlated noise from oscillations and granulation. We also include inset plots to highlight the performance of each multi-exposure strategy relative to the single continuous exposure strategy for nightly time costs of less than an hour.

on correlated noise from instrument systematics in more detail in Section 7.2.

The final noise source we consider here is photon noise. In Figure 3, we see that the multi-visit strategies are penalized more heavily due to the additional overhead costs. That is, for a given time allocation, increasing the number of visits will decrease the total exposure time and thus degrade the RV precision and achieved uncertainty on K. The single-visit strategies are again preferred across most nightly time costs. This preference is stronger for fainter stars, for which photons noise contributes a larger share of the total uncertainty.

4.3. *Inter-night Observing Schedule Simulations*

Unlike oscillations and granulation, rotationally modulated, activity-induced RV signals exhibit correlations on timescales longer than a single night. This is true for both activity GP kernels shown in Figure 2. To explore how these signals impact long term RV precision, we simulate sets of observations with one visit per night and various inter-night distributions across a typical observing season, which we assume here to be eight months, or 240 days. The following strategies are considered:

- **Uniform Sampling:** Observations are uniformly distributed across each observing season
- **Centered:** All observations occur on consecutive nights at the center of each observing season
- **Single Burst:** A mixture of the uniform and centered strategies, in which 60% of the observations take place on consecutive nights at the center of each season and the remainder are uniformly distributed
- **Double Burst:** Similar to single burst, but with two sets of consecutive nights bracketing the center of the season, each containing 30% of the observations
- **Monthly Runs:** Observations occur in equal blocks of consecutive nights at the start of each month
- **On / Off:** Observations occur in five equally spaced blocks of consecutive nights

These strategies are depicted in Figure 4. For each strategy, we build a 10 year observing schedule with annual

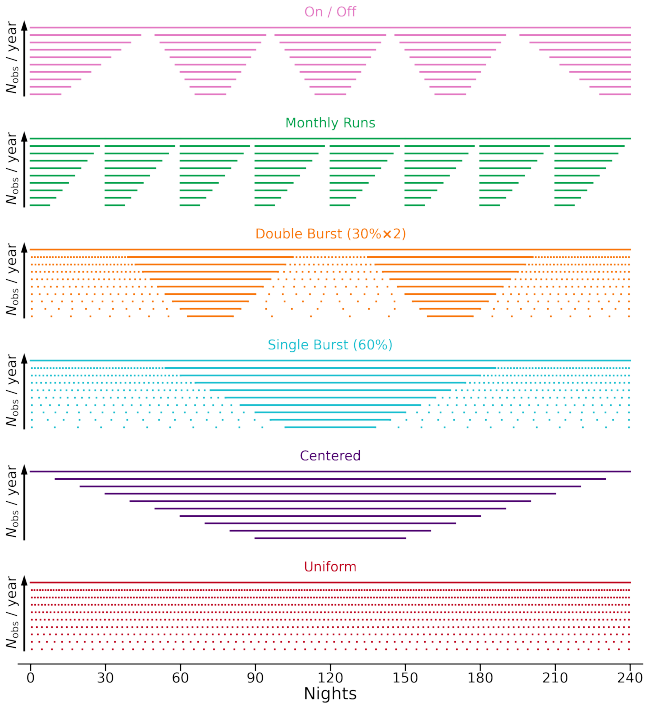


Figure 4. Simulated inter-night observing schedules over a single observing season. We show the idealized distribution of observations across a 240-night baseline for each of the strategies described in Section 4.3. Isolated points represent individual observing nights and lines represent blocks of consecutive observing nights. For each strategy, we show the distribution of observing nights for different numbers of annual observations, increasing in the vertical direction from 60 to 240 in increments of 20 observations per year.

allocations ranging from 60 observations per year to 240 observations per year, and we use Equation 4 to calculate the expected mass precision for an exoplanet with orbital parameters $K = 10$ cm s^{-1} and $P = 300$ d, again marginalizing over orbital phase as in the previous section. We calculate σ_K separately for the quasiperiodic and Matern-5/2 activity GP kernels, and we do not include any other sources of noise in the covariance matrix.

4.4. *Inter-night Observing Strategy Results*

The results from the two activity kernels show a stark contrast in the preferred strategy, the overall magnitude of σ_K, and the degree to which σ_K changes with increasing number of observations (Figure 5). When we build the covariance matrix using the quasiperiodic kernel given in Equation 15, the total length of the observing baseline is the overriding factor in determining σ_K. The Centered strategy, which uses just a fraction of the full 240-day seasonal baseline each year, performs significantly worse than the other strategies. For the other strategies, performance appears to be dictated by the uniformity of the observations across the seasonal baseline; the Uniform strategy produces the smallest uncertainty, followed by the Double Burst, Single Burst, On / Off, and Monthly schedules. But for the Matern-5/2 kernel, Equation 16, dense coverage is much more important than broad coverage. Strategies with long runs of high-cadence observations (Centered, Single Burst, Two Bursts) consistently produce the smallest σ_K for a given number of observations. And while the performance of all six strategies improves monotonically with increasing number of observations per year, these improvements are much more significant for Matern-5/2 activity kernel than for the quasiperiodic activity kernel. The predicted value of σ_K decreases by less than 7% for the best performing strategy for the quasiperiodic kernel when the number of observations increases from 60 to 240 per year, while the equivalent change in σ_K for the best performing strategy for the Matern-5/2 kernel is greater then 50%. In addition, we show that although these two kernels nominally represent the covariance behavior of the same physical process, they result in uncertainties that differ by nearly an order of magnitude regardless of observing strategy.

The differences in the predicted uncertainty for each activity kernel can be explained by their respective covariance behaviors. The Matern-5/2 kernel's negative covariance on short time scales ($\lesssim 10$ days) favors high-cadence observations, which will efficiently average out activity-induced RV variations. The covariance of the quasiperiodic kernel remains positive on all time scales, so the preferred strategies will be those with separations for which the covariance is close to zero (i.e., for which the measurements are uncorrelated). The local maximum near the stellar rotation period penalizes the Monthly strategy, for which consecutive sets of observations are separated by this same amount, and the relatively poor performance of the high-cadence Centered strategy naturally follows, as clustering all observations in the subset of a season leads to high covariance. The time scale for the covariance of the quasi-periodic kernel to fall to zero can also explain the significantly lower σ_K values we expect to retrieve for the Matern-5/2 kernel. The Matern-5/2 covariance not only reaches a white noise approximation at much smaller separations, but the negative covariance allows the activity signal to be averaged out at a rate much faster than white noise binning.

5. APPLICATION TO A REALISTIC SURVEY

Our analysis in the previous section sheds some light on the relative performance of different observing cadences both within a night and across many nights. However, the implications of the *absolute* precision we

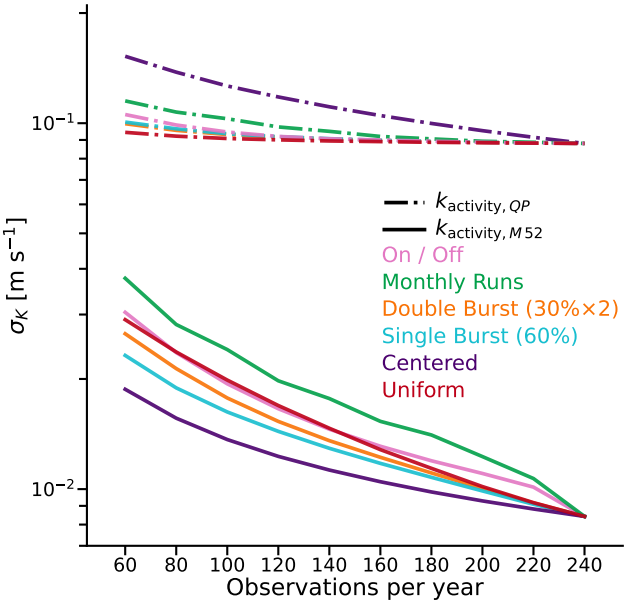


Figure 5. Expected semi-amplitude uncertainty, σ_K, for a $K = 10$ cm s^{-1} signal and an orbital period of $P = 300$ days as a function of number of observations per year. We calculate σ_K for simulated observing schedules with 10 years of observations and a 240-day annual observing season, wherein the observations for each season are distributed according to each of the strategies depicted in Figure 4 and described in Section 4.3. We include correlated noise contributions from rotationally-modulated stellar activity represented by a quasiperiodic kernel (dot-dashed lines) and by a Matern-5/2 kernel (solid lines).

report, quantified by the predicted uncertainty on K, are not as easy to interpret given that we have isolated individual noise sources. That is, these results alone do not tell us how each strategies would fare in the presence of all sources of correlated noise. In addition, we ignored practical constraints on our ability to reproduce each intended survey strategy. Real observations are subject to constraints from telescope and observatory schedules, weather losses, nightly and seasonal observing windows, and intra-survey competition. In this section, we explore how our choice of survey strategy affects sensitivity to Earth analogs in the presence of all sources of correlated stellar signals described in Section 3. Accounting for realistic observing constraints, we apply several of the strategies assessed in Section 4 to simulations of a full EPRV exoplanet survey and calculate the resulting Fisher information content.

5.1. *Survey Parameters and Target List*

As a template for our survey simulations in this work, we start with the Terra Hunting Experiment (Hall et al. 2018), an EPRV exoplanet survey that will be conducted using the soon-to-be-completed HARPS-3 spectrograph (Thompson et al. 2016). The Terra Hunting Experiment will nominally have access to 50% of the total observing time on HARPS-3 for the duration of the 10-year survey. This generous time allocation will give us ample flexibility to implement and evaluate a variety of survey strategies within our simulations.

To estimate the total time allocation for our simulated surveys, we first calculate the total annual observing time available to HARPS-3, which will be on the Isaac Newton Telescope on La Palma, Canary Islands. The mean duration of a night from this location, which we define as the time between evening astronomical twilight and morning astronomical twilight, is 9.1 hours. Assuming an annual weather loss of 16% (based on historical site statistics from La Palma; Hall et al. 2018) and that an average of 2 nights per month will be reserved for instrument, telescope, and facility maintenance, the total observing time for HARPS-3 is then 2606 hours per year. Our assumed allocation will be half of this, or 1303 hours, which we round to 80,000 minutes.

A multitude of factors will influence target selection for future EPRV Earth-analog searches, all of which should be tuned to optimize the detection of weak, sub-m s^{-1} RV signals. Gupta et al. (2021) define a set of quantitative prioritization metrics with which they identify and rank a set of stars that are conducive to EPRV exoplanet searches, i.e., bright stars with low levels of intrinsic RV variability. These metrics were used in combination with observability considerations to construct a target list for the NEID Earth Twin Survey (NETS), an ongoing EPRV exoplanet survey with the NEID spectrograph (Schwab et al. 2016) on the WIYN-3.5m telescope at Kitt Peak National observatory. The final NETS target list contains 41 stars, 40 of which are G- and K-dwarfs and one of which is an M-dwarf. We adopt the 40 Sun-like stars as our target sample for the survey simulations in this work; these stars are listed in Table 2. Although some of the NETS prioritization metrics are specific to the NEID spectrograph, we expect they are reasonably suitable for HARPS-3 given the similar spectral ranges over which the the instruments operate. In addition, these two spectrographs are at similar latitudes ($l_{\text{NEID}} = 31°57'$N, $l_{\text{HARPS-3}} = 28°46'$N), so constraints on target observability and intra-survey competition will not significantly differ.

Because correlated noise contributions from stellar variability are strongly dependent on stellar parameters, the achieved survey sensitivity is expected to be different for different sets of stars. But while Fisher information analysis can certainly be used to compare the performance of surveys with substantially different target lists,

Table 2. Target sample for survey simulations

Star Name	[a]V (mag)	[a]$T_{\rm eff}$ (K)	[a] $\log g$ ($\log$ (m s^{-2}))	[a]$M_\star$ ($M_\odot$)	Season (days)
HD4614*	3.46	5919	4.37	0.99	284
HD10700	3.49	5333	4.60	0.78	211
HD19373*	4.05	5938	4.18	1.18	275
HD26965	4.43	5092	4.51	0.79	229
HD185144*	4.67	5242	4.56	0.81	331
HD34411*	4.70	5873	4.26	1.12	271
HD115617	4.74	5562	4.44	0.94	210
HD182572	5.17	5587	4.15	1.11	287
HD201091*	5.21	4361	4.63	0.68	298
HD10476*	5.24	5190	4.51	0.84	260
HD157214*	5.38	5817	4.61	0.96	313
HD86728*	5.40	5742	4.31	1.09	268
HD143761*	5.40	5833	4.29	1.00	305
HD146233	5.50	5785	4.41	1.04	261
HD55575	5.55	5888	4.32	0.97	272
HD10780*	5.63	5344	4.54	0.90	282
HD190360*	5.70	5549	4.29	1.00	301
HD4628	5.74	4937	4.54	0.75	244
HD50692	5.76	5913	4.39	1.02	266
HD172051	5.85	5636	4.58	0.91	224
HD52711	5.93	5886	4.39	1.03	267
HD110897*	5.95	5911	4.49	0.90	294
HD186408	5.96	5778	4.28	1.08	315
HD38858	5.97	5735	4.46	0.95	236
HD187923*	6.16	5774	4.23	1.03	285
HD217107	6.18	5575	4.25	1.04	241
HD186427	6.20	5747	4.37	1.04	315
HD126053	6.25	5714	4.54	0.91	263
HD168009*	6.30	5808	4.33	1.05	321
HD127334*	6.36	5671	4.27	1.07	308
HD166620	6.38	4970	4.51	0.78	317
HD9407*	6.52	5672	4.45	1.00	286
HD179957*	6.75	5741	4.42	1.08	322
HD221354*	6.76	5221	4.47	0.86	291
HD154345*	6.76	5455	4.52	0.89	322
HD68017	6.78	5626	4.60	0.86	263
HD24496	6.81	5531	4.50	0.94	254
HD170657	6.81	5040	4.54	0.78	239
HD51419*	6.94	5732	4.51	0.90	265
HD116442	7.06	5155	4.54	0.75	254

*Included in 20-star subsample

[a]Parameters taken from Brewer et al. (2016).

we defer a detailed analysis of sample composition to future work. Here, we explore only the effects of sample size. For each of the strategies we describe in the following sections, we simulate a full 10-year survey with this 40-star target sample as well as a with a limited 20-star subsample. To select targets for the subsample, we first sort the stars by the length of their observing season, which we calculate as the number of nights for which the star can be observed with HARPS-3 at an altitude of $> 30°$ (airmass < 2) for at least 30 minutes between evening astronomical twilight and morning astronomical twilight. For this study, it is particularly important that we only consider stars with relatively long observing seasons so that we do not downplay differences between observing strategies. These differences will not be as pronounced when the total number of annual observations is a larger fraction of the available observing nights. We select the top 20 stars, then substitute several stars with slightly shorter observing seasons to improve the on-sky distribution and reduce the potential for scheduling conflicts. In Table 2 we list length of each star's observing season and we indicate which stars are included in the limited sample. Given the annual time allocation we calculated above and assuming a typical fixed time cost of 20 minutes per night each time a star is observed, we can schedule 100 observations per star per year for the 40-star sample and 200 observations per star per year for the 20-star subsample.

5.2. *Survey Strategy*

To identify a preferred survey strategy for observations within a single night, we refer back to our results in Section 4.2 and Figure 3. For our assumed time cost of 20 minutes per night, the Fisher information criterion clearly favors single visit strategies for observations of fainter stars. These strategies also perform relatively well for brighter stars, although we note that the two-visit strategy does deliver comparable precisions on this time scale. In the interest of a maintaining consistent survey strategy for all targets, we require that each star be observed just once per night. Selecting a single-visit strategy comes with the added benefit of maximizing each star's annual observing season and thereby minimizing yearly aliasing effects. For every additional hour that we require a target to be observable (i.e., to accommodate multiple visits in a night), the star's observing season is shortened by roughly one month.

For the faintest stars in our sample, overhead costs incurred by splitting a single visit into multiple exposures will significantly degrade the photon noise precision, so we would ideally adhere to a single continuous exposure for each visit. But the majority of our targets are

bright enough ($3.5 \lesssim V \lesssim 7$) that we would run the risk of saturating our detector by exposing continuously for nearly 20 minutes. We therefore schedule each visit as a sequence of three exposures with $t_{\rm exp} = 320$ seconds each, and we set $t_r = 30$ seconds and $t_{\rm acq} = 180$ seconds for a total cost of $t_{\rm night} = 20$ minutes as calculated via Equation 18. For the handful of stars in our sample brighter than $V < 4.68$, we maintain the same total time cost but divide each visit into a sequence of six exposures with $t_{\rm exp} = 145$ seconds each. This is the magnitude threshold at which a 320 second exposure of a $T_{\rm eff} = 5500$ K star would saturate the detector assuming the same cross-dispersion spread and well depth as NEID (see Section 5.4.1).

Because of the wide variation in our results in Section 4.4, we consider four different inter-night strategies for our survey simulations. These include the best- and worst-case strategies for the quasiperiodic and Matern-5/2 activity kernels (Uniform, Centered, and Monthly) as well as the Double Burst strategy as an intermediate reference point. We implement each strategy within our scheduling framework, which we describe in the following subsection, by creating custom binary masks that specify allowed and disallowed observing nights for each star. For the Centered strategy, for example, all nights in the middle of a star's observing season are allowed while those at the edges are disallowed, and for the Uniform strategy, the allowed nights are uniformly spaced. To ensure that we end up with the intended number of observations per star after accounting for practical constraints, the number of allowed nights each year exceeds the intended annual total by 20-30% (e.g., ~ 125 nights per star for the 40-star sample or ~ 250 nights per star for the 20-star sample).

5.3. *Survey Schedule Simulations*

To construct each simulated survey, we start by building a 10-year series of nightly observing schedules. Though we do use custom binary masks for each star to emulate the intended inter-night strategy for the survey, we assume no prior knowledge of weather losses or other constraints on when observations can be scheduled. For each night, we schedule observations for the set of allowed targets in order of increasing time of peak altitude. That is, the first star to be added to the schedule will be the star that reaches its highest altitude closest to evening astronomical twilight. If two stars reach their peak at the same time (e.g., stars that are already setting at twilight), priority is given to the star that is lower in the sky at this time. Observations are scheduled at the time of peak altitude. We record the start time and duration of each exposure, and a 180 second acquisition time is blocked off at the end of each sequence so that each observation consists of a contiguous 20 minute block. Any subsequent observation that would overlap with one that was previously scheduled is shifted in time until the start time of the observation coincides with the end of the previous block. We continue to add observations to the schedule in this manner until an observation crosses midnight. At this point, we repeat the process in reverse, starting with morning astronomical twilight and working backwards until we again hit midnight. If the start time of an observation would be shifted by more than 3 hours from the time of peak altitude or if the airmass at the time of observation would exceed 2, the observation will not be scheduled on that night. Scheduling observations in this manner will necessarily leave gaps in the night, as there will often be more than 20 minutes between consecutive peak altitude times for the stars on our target list. But these gaps are an important feature of the simulated schedule, as they naturally represent the effect of competition with other observing programs. Because our hypothetical survey has access to only 50% of the available observing time, we should not expect to pack the schedule each and every night, and there will frequently be instances when available targets are not observed.

After the schedule is generated, we mask a fraction of the nights to account for anticipated observing losses. We first consider observing nights lost to weather. Taking the binary mask constructed by Hall et al. (2018) based on historic weather losses at La Palma, we calculate the average fraction of nights lost to weather during each calendar month, f_m. For each scheduled night, we then compare the corresponding f_m value to a randomly generated number f_w on the interval $0 \leq f_w < 1$. The following criteria are used to determine which parts of each night to mask, if any:

$$0 \leq f_w < \tfrac{1}{2} f_m \implies \text{full night masked}$$

$$\tfrac{1}{2} f_m \leq f_w < f_m \implies \text{first half masked}$$

$$f_m < f_w \leq \tfrac{3}{2} f_m \implies \text{last half masked}$$

$$\tfrac{3}{2} f_m \leq f_w < 1 \implies \text{full night open.}$$

In practice, this adds some granularity to the weather losses without changing the average time we would lose per month if we simply masked all nights for which $0 \leq f_w < f_m$.

Even when the telescope is open, we expect some observing time will be unavailable for high precision RV measurements when the seeing is poor. In poor seeing conditions, guiding errors will introduce additional RV uncertainty and the flux captured by the fiber will decrease, degrading the achieved photon noise precision.

To simulate seeing losses, we naïvely assume seeing is constant throughout each night and we draw values from the following Rayleigh distribution

$$P(\mathrm{FWHM};\sigma) = \frac{\mathrm{FWHM}}{\sigma^2} e^{-\mathrm{FWHM}^2/(2\sigma^2)} + 0.5 \qquad \sigma = 0.68 \tag{19}$$

with a median full-width half-max (FWHM) of 1.3″ to match empirical conditions at the Isaac Newton Telescope (Thompson et al. 2016) and a minimum of 0.5″. We set an upper tolerance on the seeing FWHM of 2.5″ and mask all nights for which the seeing exceeds this limit. Finally, to simulate a maintenance schedule, we mask two randomly selected nights out of every month. All observations in any of these masked windows are then dropped from the schedule. We note that these masks are not expected to be mutually exclusive, so they are all drawn independently and will therefore overlap to some degree. In Figure 6, we show the first two years of observations and anticipated losses for one of our simulated survey schedules.

5.4. *RV Noise Contributions*

As in Section 4, we do not need to generate RV measurements to accompany our simulated survey schedules. The Fisher information content does not depend on the measurements themselves. However, we do need to account for the associated noise properties. Here, we describe the computation of the covariance matrix for each target star, accounting for all four sources of noise in Equation 11.

5.4.1. *Photon Noise*

Photon noise contributes a diagonal term to each stars covariance matrix. The photon noise precision of an exposure, σ_{photon}, depends on the RV information content of the observed spectrum as described by Bouchy et al. (2001). For observations with a given spectrograph, the precision will vary as a function of the spectral type of the star and the achieved SNR, which in turn depends on the exposure time, stellar brightness, and observing conditions. To determine σ_{photon} for our simulated observations, we first calculate the expected SNR as a function of T_{eff}, V-band magnitude, and exposure time using the NEID exposure time calculator. We then apply two multiplicative corrections to account for the simulated seeing conditions (Equation 19) and for the effective system throughput of HARPS-3 relative to NEID

$$\mathrm{SNR}_{\mathrm{scaled}} = \mathrm{SNR}\sqrt{R_{\mathrm{seeing}} R_{\mathrm{system}}}. \tag{20}$$

The seeing correction is calculated by taking the cross section of the fiber (on-sky diameter $d_f = 1.4''$; Thompson et al. 2016) and the seeing disk, assuming that the star is perfectly centered

$$R_{\mathrm{seeing}} = \frac{1 - e^{-\frac{1}{2}\left(\frac{d_f/2}{\mathrm{FWHM}/2.355}\right)^2}}{1 - e^{-\frac{1}{2}\left(\frac{d_f/2}{\mathrm{FWHM}_{\mathrm{median}}/2.355}\right)^2}}, \tag{21}$$

and comparing this to the same cross section in median seeing conditions ($\mathrm{FWHM}_{\mathrm{median}} = 1.3''$). To scale the throughput, we calculate the photon noise precision we would expect to achieve for some test values of R_{system}, and find we can match the HARPS-3 results calculated by Thompson et al. (2016) if we apply a correction factor of $R_{\mathrm{system}} = 1.375$. However, Thompson et al. (2016) assume a fairly conservative system throughput of 5%. Here, we assume a more optimistic 10% average efficiency, so we set $R_{\mathrm{system}} = 2.75$. The final photon noise is then estimated from $\mathrm{SNR}_{\mathrm{scaled}}$ using the NEID exposure time calculator as described in Gupta et al. (2021). We note that for NEID, the detector saturates at SNR≈ 625. In median seeing conditions, we find that $\mathrm{SNR}_{\mathrm{scaled}}$ will exceed this threshold in a 320 second exposure for stars brighter than $V = 4.68$, hence our decision to use shorter exposures for the brightest stars in our sample.

5.4.2. *Stellar Variability*

We calculate the correlated noise contributions from stellar variability using Equations 12 and 14 for oscillations and granulation, respectively, again integrating over the exposure time as in Section 4.1, and using Equations 15 and 16 for spot-induced activity. In Section 4, we assumed perfectly solar hyperparameters as given in Table 1. We continue to assume Solar values for the activity kernels here, but to enable a more even comparison of their absolute performance, we set the amplitude of the quasiperiodic kernel to be $\alpha = 0.6$ m s^{-1} such that it matches that of the Matern-5/2 kernel at $\Delta = 0$. For the asteroseismic signals, we take advantage of known stellar parameter scaling relations (given in Luhn et al. 2023) to estimate more accurate oscillation and granulation kernel hyperparameters for each of our target stars. As inputs to these scaling relations, we take spectroscopically derived effective temperatures, T_{eff}, and surface gravities, $\log g$, from Brewer et al. (2016). These stellar parameters are listed in Table 2. For each simulated survey schedule, we treat the two activity kernels independently just as we did in Section 4, computing separate covariance matrices and analyzing separate sets of results.

6. RESULTS

6.1. *Detection Sensitivity and Survey Success Metrics*

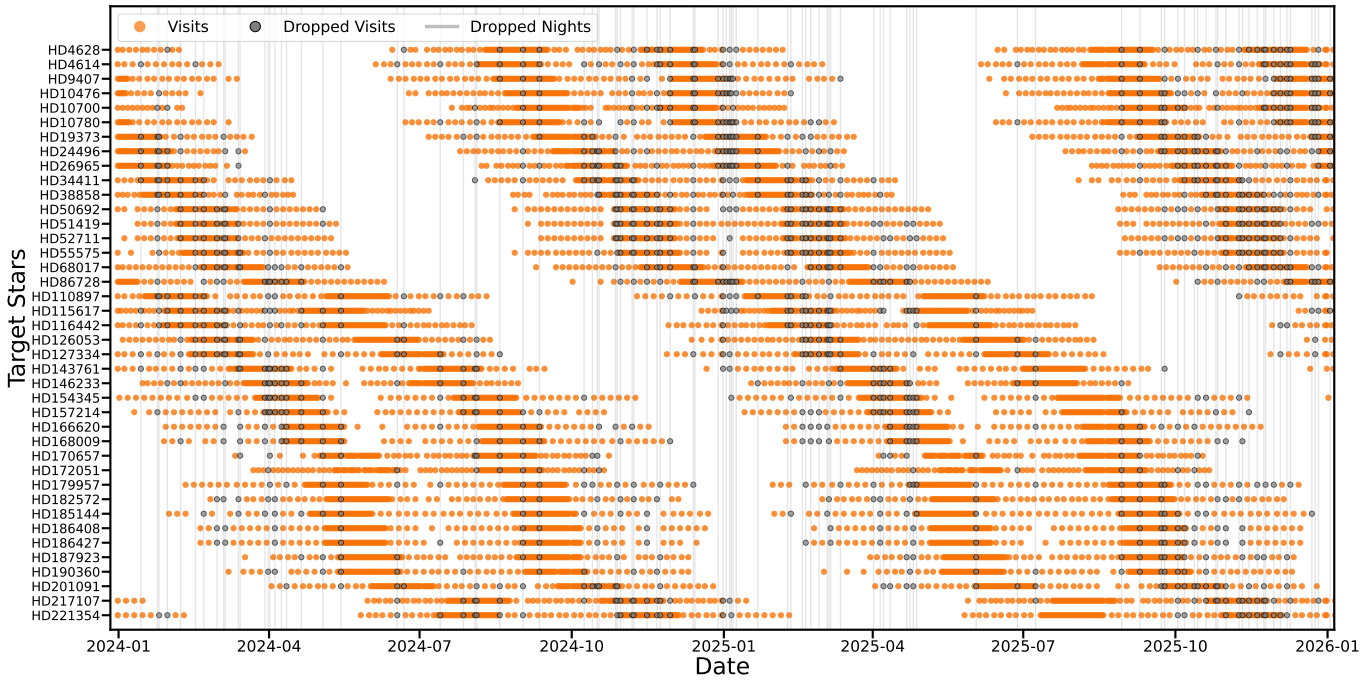


Figure 6. First two years of simulated observations for the Double Burst inter-night observing strategy as applied to the 40-star target sample with practical constraints on target observability. Stars are shown in order of increasing RA from top to bottom. Orange markers represent nights during which each target was observed, grey markers show observations that were scheduled and then dropped due to simulated weather losses and telescope closures, and grey lines indicate the nights on which these losses occurred. For most stars, we are able to achieve a reasonable approximation of the idealized version of this strategy shown in Figure 4 in spite of these practical constraints.

With the simulated schedules and covariance matrices in hand, we can use Equations 4 and 5 to calculate σ_K and assess the achieved sensitivity of each survey strategy. We first compute K as in Equation 6 for a broad range of $M_p \sin i - P$ parameter combinations, assuming circular orbits and taking stellar masses from Brewer et al. (2016), and then we calculate σ_K for the corresponding parameter vector θ, marginalizing over orbital phase at each point. We use these results to determine the expected detection significance, K/σ_K, which we show for two representative cases in Figure 7.

To compare performance across different survey strategies, we define two quantitative success metrics. The first metric is simply the detection significance for an Earth analog, $[K/\sigma_K]_\oplus$. Here, we define an Earth analog to be a $M_p \sin i = M_\oplus$ exoplanet with an orbital period of 300 days (green 'x' in Figure 7). We choose $P = 300$ days rather than $P = 365$ days so as not to bias our results against strategies that are more susceptible to annual aliasing. For each simulated survey, we calculate and tabulate (Table 3) the number of stars for which the detection significance exceeds a threshold H, i.e., $N_{[K/\sigma_K]_\oplus > H}$, setting $H = [3, 5, 10]$ for the Matern-5/2 activity kernel results and $H = 1$ for the quasiperiodic kernel results. We also show the distribution of $[K/\sigma_K]_\oplus$ values for each simulated survey in Figure 8.

We adopt a slightly looser definition of an Earth analog for our second success metric, $D_\oplus$, which we will refer to integrated Earth analog discovery space:

$$D_\oplus = \int_{P_{\rm min}}^{P_{\rm max}} \log\left(\frac{2M_\oplus}{M_{p,\rm min}}\right) d\log P. \tag{22}$$

We set $P_{\rm min} = 200$ days and $P_{\rm max} = 500$ days and we calculate the minimum detectable mass, $M_{p,\rm min}$, as

$$M_{p,\rm min} = \begin{cases} 0.5M_\oplus & [M_p \sin i]_H < 0.5M_\oplus \\ [M_p \sin i]_H & [M_p \sin i]_H \geq 0.5M_\oplus \end{cases} \tag{23}$$

where $[M_p \sin i]_H$ is the mass at which $K/\sigma_K = H$ for a given orbital period. We again set thresholds of $H = 3$, 5, and 10 for the Matern-5/2 activity kernel and a $H = 1$ threshold for the quasiperiodic activity kernel. By expanding our definition of an Earth analog to include all exoplanets with 200 days $< P <$ 500 days and $0.5M_\oplus < M_p \sin i < 2M_\oplus$, as shown by the green box in Figure 7, we reduce our sensitivity to small K/σ_K fluctuations in $M_p \sin i - P$ space.For each simu-

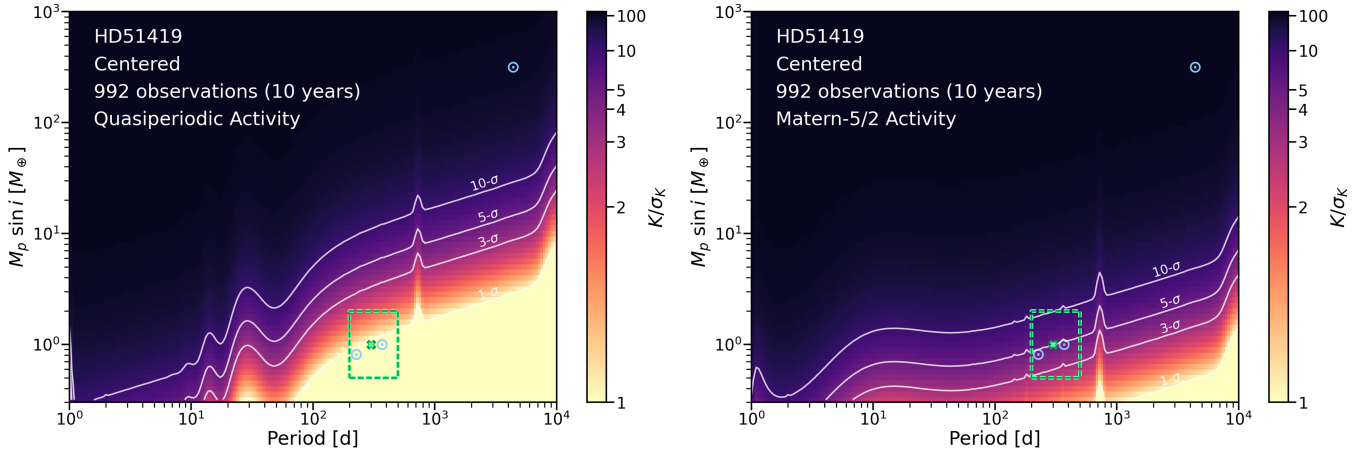


Figure 7. Expected exoplanet detection sensitivity limits as calculated using our Fisher information framework for a typical target star with approximately 100 observations per year for 10 years and the Centered inter-night observing strategy. We include contributions from photon noise, oscillations, granulation, and stellar activity. We plot K/σ_K as a function of minimum mass, $M_p \sin i$, and orbital period, P. For reference, we also plot the 3-, 5-, and 10-σ detection significance contours and we indicate the locations of the Solar System planets Venus, Earth, and Jupiter with the $\odot$ symbol. The green 'x' and green dashed box indicate the mass and period values and ranges we use to define an Earth analog for the $[K/\sigma_K]_\oplus$ and $D_\oplus$ survey success metrics, respectively. Results for the quasiperiodic activity kernel are shown on the left and results for the Matern-5/2 activity kernel are shown on the right.

Table 3. Survey Simulation Success Metrics

Activity Kernel	Metric	Centered (40 stars)	Centered (20 stars)	Uniform (40 stars)	Uniform (20 stars)	Monthly (40 stars)	Monthly (20 stars)	Double Burst (40 stars)	Double Burst (20 stars)
Quasiperiodic	$N_{[K/\sigma_K]_\oplus>1}$	5	19	38	20	25	19	38	20
Matern-5/2	$N_{[K/\sigma_K]_\oplus>3}$	40	20	40	20	38	20	40	20
Matern-5/2	$N_{[K/\sigma_K]_\oplus>5}$	21	19	22	19	4	18	17	19
Matern-5/2	$N_{[K/\sigma_K]_\oplus>10}$	0	2	0	1	0	1	0	2
Quasiperiodic	$\sum D_\oplus(H=1)$	392	279	584	301	512	290	574	300
Matern-5/2	$\sum D_\oplus(H=3)$	836	480	828	477	676	474	793	479
Matern-5/2	$\sum D_\oplus(H=5)$	488	367	478	357	313	347	434	363
Matern-5/2	$\sum D_\oplus(H=10)$	65	126	60	115	5	107	40	121

lated survey, we sum over $D_\oplus$ for all stars and show the results in Table 3.

6.2. *Survey Strategy Performance Comparison*

In the case that our stellar activity model is best represented by the quasiperiodic kernel given in Equation 15, none of the survey strategies tested here are expected to yield detections of Earth analogs at the $[K/\sigma_K]_\oplus > 1.5$ significance level (Figure 8). We note that such a marginal detection significance would be unconvincing, especially given the high standards for evidence one would expect for such an important discovery. We comment on this further in Section 7.1. Here, we focus on the relative performance of the different strategies for this assumed activity model. As we show in Table 3 and Figure 8, the $N_{[K/\sigma_K]_\oplus>1}$ success metric is fairly sensitive to our choice of survey strategy for the full 40-star sample. While nearly every star reaches the $[K/\sigma_K]_\oplus > 1$ threshold for the Uniform and Double Burst strategies, far fewer stars reach this threshold for the Monthly strategy and only a handful do for the Centered strategy. Yet in the case of the 20-star subsample, this performance gap is nearly erased, and nearly every star reaches the $[K/\sigma_K]_\oplus > 1$ threshold for all strategies. This is entirely consistent with our interpretation of the results in Section 4.4. For this activity kernel, the achieved detection sensitivity is strongly correlated with the length of the observing baseline within each ob-

serving season. Whereas the Uniform and Double Burst strategies will always span the entire season, the Centered strategy sacrifices a longer baseline for a higher observing cadence. But as the number of observations per year approaches the total number of available nights (i.e., for the 20-star sample with 200 observations per star per year), the strategies become indistinguishable. We also highlight the almost negligible change in the distribution of $[K/\sigma_K]_\oplus$ values between the 40-star and 20-star samples for the Uniform and Double Burst strategies, despite the latter sample having twice the number of observations per star (Figure 8). Just as in Figure 5, the increased number of observations only significantly benefits the Centered strategy, for which this increase also translates to a greatly extended annual baseline.

For the Matern-5/2 activity kernel, the $N_{[K/\sigma_K]_\oplus > H}$ success metric tells a different story. First, we note that the absolute performance of each survey strategy is significantly more encouraging, as nearly every star reaches the $H = 3$ threshold for all simulated survey strategies and even the $H = 5$ threshold for each of the 20-star simulations. And while only half of the observed stars reach $[K/\sigma_K]_\oplus > 5$ for the 40-star simulations with the Centered, Uniform, and Double Burst strategies, each of these strategies will still yield close to 20 stars that are sensitive to Earth analogs at this level. The relatively poor performance of the Monthly strategy here is consistent with our results in Section 4.4, as is the lack of variation from strategy to strategy for the 20-star sample. But it is surprising that the Centered strategy fails to outpace the Uniform and Double Burst strategies for the 40-star sample; Figure 5 clearly shows that the Centered strategy performs significantly better for schedules with just 100 observations per year. The difference between the results presented here and those presented in Section 4.4, which uses an idealized observing schedule, likely stems from the practical constraints imposed on the full survey simulations. By restricting the available observing nights to account for these constraints, we have effectively extended the annual observing baseline of the Centered strategy such that it is no longer as distinct.

The larger sample size of 40 stars will be preferred for a survey with a target detection threshold of $H = 3$. But as H increases to $H = 5$ and again to $H = 10$, $N_{[K/\sigma_K]_\oplus > H}$ drops off much more steeply for the 40-star sample than for the 20-star sample. This same effect is illustrated in Figure 8, which shows that the average detection significance is significantly higher for the 40-star sample, thus demonstrating that preferred sample size is inversely proportional to the stringency of our detection significance requirements. This is in stark contrast to our interpretation of the $N_{[K/\sigma_K]_\oplus > H}$ success metric for the quasiperiodic kernel, for which we see only a marginal increase in detection significance when we reduce the sample size and double the number of observations per target.

The results of the two success metrics in Table 3 are largely consistent with each other, but there are several notable differences that we highlight here. For both kernels, the $D_\oplus$ success metric paints a more granular picture of relative survey strategy performance. This is most pronounced for the Matern-5/2 kernel at the $H = 5$ detection significance level. The ≈ 20 stars in the 40-star sample that do not reach $[K/\sigma_K] > 5$ for a $1 M_\oplus$, 300-day planet can still reach this threshold for planets with slightly larger masses and shorter orbital periods that still fall within the expanded Earth analog parameter bounds we defined in Section 6.1. But $\sum D_\oplus$ does not have as much room to grow for the 20-star sample, for which nearly every star already exceeds the $[K/\sigma_K]_\oplus > 5$ threshold. As a result, the value of $\sum D_\oplus$ is $\approx 25\%$ larger for the 40-star sample than for the 20-star sample at $H = 5$ even though both samples yield $N_{[K/\sigma_K]_\oplus > 5} \approx 20$ for each of the Centered, Uniform, and Double Burst strategies. The smaller sample does eventually overtake the larger sample as H increases, but the change in preferred sample size occurs at a larger detection significance threshold than the $N_{[K/\sigma_K]_\oplus > H}$ results suggest.

6.3. *Cadence vs. Baseline*

The factors driving the relative performance of the survey strategies explored here can largely be distilled into to three key parameters. These are the frequency with which each star is observed, the total number of stars in the sample, and the observing baseline for each star both within each season and across the entire survey. Within the constraints of a survey with a fixed total time allocation, these parameters cannot be independently tuned. But we can still examine how our results change when two or more parameters are adjusted. Indeed, we have already discussed the trade-off between sample size and cadence and shown that results for the two activity kernels are at odds with each other. For the quasiperiodic kernel, increasing the cadence adds little value and is not worth the decrease in sample size, while for the Matern-5/2 kernel, a higher cadence and smaller sample size is increasingly preferred as we raise our target detection significance threshold.

To shed light on the trade-off between observing cadence and total survey baseline, we re-compute the Fisher information and resulting $[K/\sigma_K]_\oplus$ values for each of the 20-star survey simulations using just the first

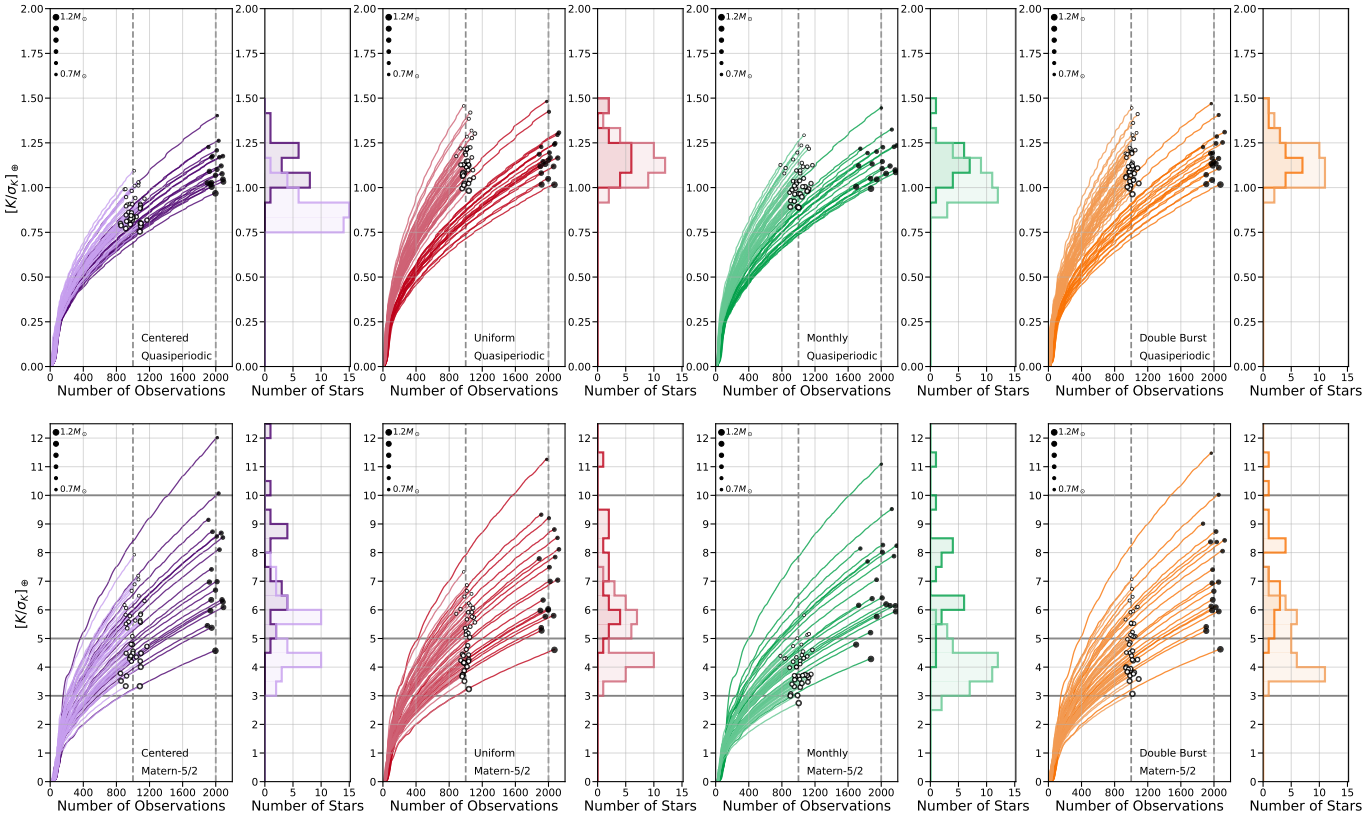


Figure 8. Expected Earth analog detection significance, $[K/\sigma_K]_\oplus$, as a function of number of visits for each of our survey simulations. The darker lines that terminate in filled circles correspond to the results for the 20-star simulations and the lighter lines that terminate in open circles correspond to the results for the 40-star simulations. The size of each circle scales with stellar mass. We note that each of these lines is exhibits a relatively smooth dependence on number of observations within an observing season, but that these smooth changes are interrupted by sharper kinks between observing seasons. Dashed vertical lines mark the expected number of observations per star for an idealized observing schedule, i.e., 1000 total observations for each of the 40-star simulations and 2000 total observations for each of the 20-star simulations. The final distributions of $[K/\sigma_K]_\oplus$ values for each survey are shown as histograms in the narrow panels to the right side.

5 years of observations for each star. By fixing the total number of observations to about 1000 per star, we can directly compare these results the results for these same stars over the full 10-year duration of the 40-star survey simulations. As Figure 9 shows, our strategy recommendation will again depend on the assumed activity kernel. For the quasiperiodic model, the longer 10-year survey outperforms the shorter 5-year survey for all strategies, and for the Matern-5/2 kernel the shorter, higher-cadence survey wins out. In both cases, the Centered observing strategy is shown to be least sensitive to this trade-off between baseline and cadence. This is consistent with expectations given that changing the number of observations for this strategy serves only to adjust the length of the baseline within each season rather than the frequency of observations.

Based on our results, the preferred survey strategies differ significantly for each of the two activity kernels we have applied, as does the absolute detection significance we can expect to achieve. But when interpreting these results, one should be careful not to attribute the differences purely to the kernel forms. As we show in Figure 2 and Table 1, we assume significantly different correlation length hyperparameters for the quasiperiodic and Matern-5/2 kernels. While the form of each kernel undoubtedly plays a role in the resulting detection sensitivities, the stark contrast we predict could likely be reduced by adjusting these hyperparameters. We comment on this further in the following section.

7. DISCUSSION

7.1. *Stellar Variability Model Assumptions*

One shortcoming of the work presented herein is that our analysis framework implicitly assumes perfect knowledge of the stellar variability kernels and their hyperparameters with which we construct the covariance matrices for our Fisher information calculations. The target lists for ongoing EPRV exoplanet searches are selectively composed of intrinsically "quiet" stars (Brewer et al. 2020; Gupta et al. 2021), as is the target list used

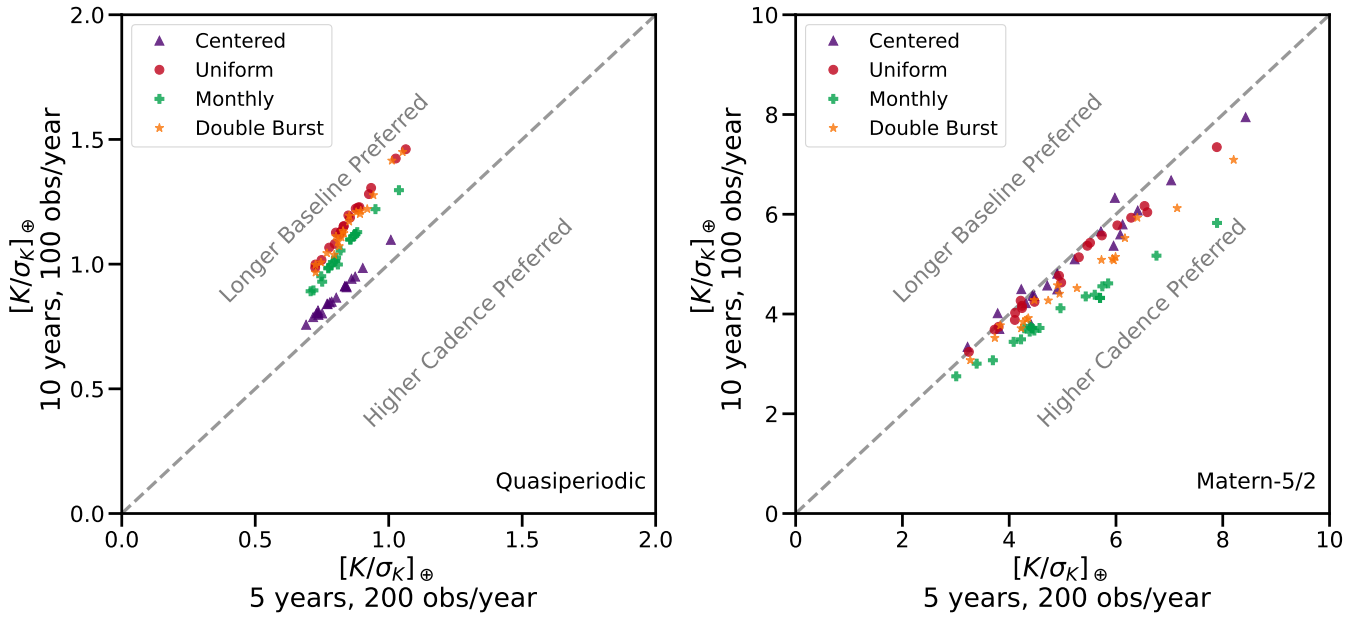


Figure 9. Comparison of $[K/\sigma_K]_\oplus$ for a 10-year survey with 100 observations per year (vertical axis) and a 5-year survey with 200 observations per year (horizontal axis). We compute the latter values using the first 5 years of observations from the 20-star survey simulations. On the left, we show that for the quasiperiodic kernel, the longer 10-year survey delivers a higher detection significance than the higher cadence 5-year survey. On the right, we show that the opposite is true for the Matern-5/2 kernel, which performs better with a higher observing cadence.

for the survey simulations in this work. This is advantageous in that it naturally reduces the impact of variability on exoplanet detection, but it has also limited our ability to directly measure and model these stars' intrinsic variability signals, as the amplitudes of these signals are at a level below the precision floor achieved by surveys with older spectrographs. As such, the stellar variability models we use here are informed primarily by Solar observations and models and, in the case of oscillations and granulation, extended to other stars via scaling relations. While physically motivated, these scaling relations are not perfectly accurate, and oscillation and granulation timescales and amplitudes will often depend on additional stellar physics that these relations do not capture (Cattaneo et al. 2003; Jiménez-Reyes et al. 2003; Bonanno et al. 2014; García et al. 2014; Mathur et al. 2019; Gupta et al. 2022). The results of our stellar activity kernel analysis should be treated with caution as well, as we assume perfectly Solar hyperparameters for these kernels throughout our analysis. Stars with different rotation periods or different characteristic spot lifetimes will likely favor different internight survey strategies. For example, we note that the 28-day Solar rotation period is particularly disadvantageous for the Monthly observing strategy, as this strategy will consistently sample roughly the same phase of the rotationally-modulated activity signal. That is, the interpretation of the poor performance of this strategy in our simulations should be that we should avoid observing cadences that are synchronized to the stellar rotation period. And while it has been shown that scaling relations can be used to predict rotation periods in lieu of empirical measurements (e.g., Baliunas et al. 1983; Suárez Mascareño et al. 2015), these predicted periods are too imprecise for Sun-like stars to inform the results of studies such as this.

If we aim to accurately predict the achievable detection sensitivity for specific stars, we must make an effort to empirically measure and model stellar signals for these stars at the sub-m s^{-1} level. Fortunately, ongoing EPRV surveys and other targeted observing campaigns are building the data sets that will enable these empirical measurements for the first time. Collaborative efforts such as the EXPRES Stellar Signals Project (Zhao et al. 2020, 2022), in which data sets are analyzed by multiple teams with suites of RV analysis techniques, are particularly promising. Analyses that make use of archival data to measure long-term stellar activity cycles (e.g., Baum et al. 2022) will also be instrumental for accurate estimation of the activity-induced correlated noise contributions for EPRV surveys that last as long as 10 years.

In addition, the differences between the two sets of results we present for the Matern-5/2 activity kernel and quasiperiodic activity kernel highlight the sensitivity of this analysis to each assumed kernel form. Depending

on which kernel we use to represent and model stellar activity, there is a marked change in the absolute detection significance we can expect to achieve as well as in our interpretation of the preferred survey strategy. For the quasiperiodic kernel, we would not expect to make a significant detection of an Earth analog with any of the simulated surveys despite the generous number of observations allotted to each star. This is in part be a consequence of the hyperparameters we assume for each kernel, but the covariance behavior we discuss in Section 4.4 plays a role as well. Recent work by Gilbertson et al. (2020b) and Nicholson & Aigrain (2022) using simulated data has shed some light on the efficacy of different types of kernels in modeling and removing stellar signals, but we again emphasize the need to apply these types of analyses to real data for specific stars.

We also note that we have assumed that each of the stellar variability kernel hyperparameters are not only perfectly accurate, but also perfectly precise. Even if one were to apply this analysis to stars with well constrained asteroseismic and activity signals, the resulting orbital parameter uncertainties would not include propagated uncertainties on the measured correlated noise hyperparameters. Extending this framework to accommodate hyperparameter uncertainties once empirical models are in hand will improve the accuracy of our results and enable us to quantify how tightly the kernel hyperparameters need to be constrained to adequately model out stellar variability signals and enable Earth analog exoplanet detection.

7.2. *Accounting for Instrumental Noise*

We have chosen to ignore noise contributions from spectrograph and pipeline systematics in this study so that we could isolate the effects of other sources of noise and assess relevant mitigation strategies. As we state in Section 3, we assumed to first order that well-understood instrumental variations are calibrated out prior to computing the RV time series from observed stellar spectra, and we ignore residuals and other poorly understood systematic signals that remain. A thorough discussion of the cumulative covariance contributions from numerous sub-m s^{-1} instrument systematics is well beyond the scope of this work, but it is worth considering their impact on our conclusions.

We repeat the Fisher information analysis for our intra-night observing schedule simulations in Section 4 with the addition of a single instrumental covariance contribution that is constant for all observations taken within a single night and perfectly uncorrelated across multiple nights. Noise such as this might stem from variations in a wavelength solution that is anchored to a nightly calibration sequence. This covariance contribution can be represented by a simple step function kernel:

$$k_{\rm instrument}(\Delta) = \begin{cases} \sigma^2_{\rm instrument} & \Delta \leq 0.5 \text{ days} \\ 0 & \Delta > 0.5 \text{ days.} \end{cases} \quad (24)$$

We perform this analysis for internal single epoch precisions of $\sigma_{\rm instrument} = 30$ cm s^{-1} and $\sigma_{\rm instrument} = 10$ cm s^{-1}, where the former is based on recent best estimates for current generation EPRV spectrographs (Halverson et al. 2016; Blackman et al. 2020) and the latter is an optimistic projection for future instruments. As expected, the addition of $k_{\rm instrument}$ to our covariance matrix neither changes the preferred intra-night observing strategy nor accentuates any differences between strategies. Because the covariance timescale is set such that each simulated schedule receives the same number of independent epochs, this instrumental noise contribution serves only to raise the achieved precision floor for all strategies. We find that the increase in σ_K can be approximated as

$$\sigma_K^2 \approx \sigma_K^2 + 2\sigma^2_{\rm instrument}/N_{\rm nights}. \quad (25)$$

This will have a negligible effect on sensitivity to Earth analogs when σ_K is on the order of 10 cm s^{-1} or greater (e.g., for our full simulation results using the quasiperiodic activity kernel). But even with thousands of observations and an instrumental precision of $\lesssim 30$ cm s^{-1}, this can significantly degrade the achieved Earth analog detection significance when $[K\sigma_K]_\oplus \gtrsim 5$ (e.g., for our results using the Matern-5/2 activity kernel). Future studies that account for realistic instrumental noise contributions in simulations such as those discussed in Section 5 are strongly encouraged.

7.3. *Stellar Mass Dependence*

As we show in Figure 8, each of our survey simulations yields a broad distribution of $[K/\sigma_K]_\oplus$. Differences in each of our survey success metrics from star to star can partly be attributed to the dependence of the RV semi-amplitude on stellar mass, $K \propto M_\star^{-2/3}$, which shows that we typically expect to achieve better sensitivity to exoplanets orbiting low mass stars. To study this dependence in more detail, we show the achieved detection significance as a function of stellar mass in Figure 10. For each survey simulation, we also plot a $M_\star^{-2/3}$ curve with a fitted offset, i.e., $[K/\sigma_K]_\oplus = M_\star^{-2/3} + \text{offset}$. While this relation appears to be a reasonably good approximation for the quasiperidic activity kernel results, the Matern-5/2 kernel results exhibit a much steeper dependence on stellar mass. This steeper slope suggests

that σ_K depends on stellar mass as well when we use the Matern-5/2 kernel. Luhn et al. (2023) see a similar trend in their survey analysis results and arrive at the conclusion that this is a consequence of the stellar parameter dependence of the oscillation and granulation correlated noise signals. Low-mass stars thus carry even more of an advantage for low-mass exoplanet detection than the RV semi-amplitude scaling would suggest. We note that this effect is only observed in the Matern-5/2 activity kernel results because the correlated noise contributions from the quasiperiodic activity kernel are so large that they mask any strong dependence on the asteroseismic correlated noise.

7.4. *Sensitivity to assumed definition of an Earth analog*

Our definition of an Earth analog as applied to the $D_\oplus$ survey success metric is somewhat arbitrary and does not fully capture the commonly cited objective of ambitious EPRV surveys, which is to detect and measure the masses and orbits of Earth-mass planets in the Habitable Zones of their host stars (Crass et al. 2021). Because we fix the period range to 200 days $< P <$ 500 days for all stars, we do not account for the change in the location of the Habitable Zone as a function of stellar luminosity. Similar arguments can be made to change our mass limits of $0.5M_\oplus < M_p \sin i < 2M_\oplus$. However, we show in Figure 11 that while certain features in the detection significance contours are more pronounced for some strategies than for others, the local slope of these contours over our specified period and mass ranges is quite insensitive to survey strategy. Instead, the differences between the success metrics calculated for each strategy result primarily from linear displacements of the detection significance levels. Changing the boundaries or even the shape of the region we use to calculate $D_\oplus$ will therefore have little to no effect on the relative performance of different survey strategies.

7.5. *RV Model Complexity*

In this work, we employ a simplified model for the exoplanet-induced RV signal, assuming only one planet with a circular orbit. While our model allows us to focus on and compare specific survey strategy choices, future investigations in this vein could benefit from additional model complexity. For example, one might explore how the Fisher information changes for several representative eccentricity values instead of assuming a circular orbit, or even quantify the effect of marginalizing over an empirical eccentricity distribution (e.g., Kipping 2013; Van Eylen et al. 2019).

Our approach also implicitly assumes perfect knowledge of γ, the absolute RV of the stellar rest frame, and of the RV signals imparted by any other exoplanets in the same system as the nominal Earth analog we are interested in detecting. In the case that γ is the same for all observations, it can be accounted for by adding a constant offset term to Equation 7, and it will not substantially affect the Fisher information calculation. But in practice, it is often necessary to combine data from multiple instruments to enable the detection of RV signals from low-mass, long-period exoplanets. The slight differences in the absolute RV scale for each instrument will necessitate the inclusion of instrument-specific γ terms. A time-dependent γ term can also be used to account for RV zero-point offsets in the data stream from a single instrument, such as those introduced by the SOPHIE octagonal fiber upgrade (Bouchy et al. 2013) or the HIRES detector upgrade. It is not unreasonable to expect that the HARPS-3 spectrograph will experience an upgrade of this sort over the course of the 10-year Terra Hunting Experiment. Post-survey detection sensitivity analyses should take care to explicitly account for a varying γ term.

The assumption that we will have detected and characterized all other significant exoplanet-induced signals in each system is also likely too optimistic. First, we note that several studies have found evidence for elevated co-occurrence rates for inner terrestrial planets and cool gas giants (Bryan et al. 2019; Rosenthal et al. 2022) and multi-planet systems in general have been shown to be fairly common (Fang & Margot 2012; Zhu 2022). While EPRV surveys may easily detect and characterize a Jupiter analog with a $K \sim 10$ m s^{-1}, uncertainties on the mass and orbit will still complicate the detection of smaller RV signals. In addition, signals from multiple small planets with orbital periods close to 1 year, e.g., an Earth analog and a Venus analog, may be particularly difficult to disentangle. Expanding our RV model to account for signals from multiple planets within the Fisher information framework will enable us to determine the magnitude of this effect on Earth analog detection.

8. CONCLUSIONS

We outline a detailed framework for analyzing the detection sensitivity of EPRV exoplanet surveys and we use this to assess the efficacy of various survey strategies in the correlated noise dominated regime. By using Fisher information analysis to quantify the impact of intrinsic stellar variability on exoplanet detection we can capture these correlated noise contributions with GPs and we circumvent the need to synthesize and fit RV time series measurements.

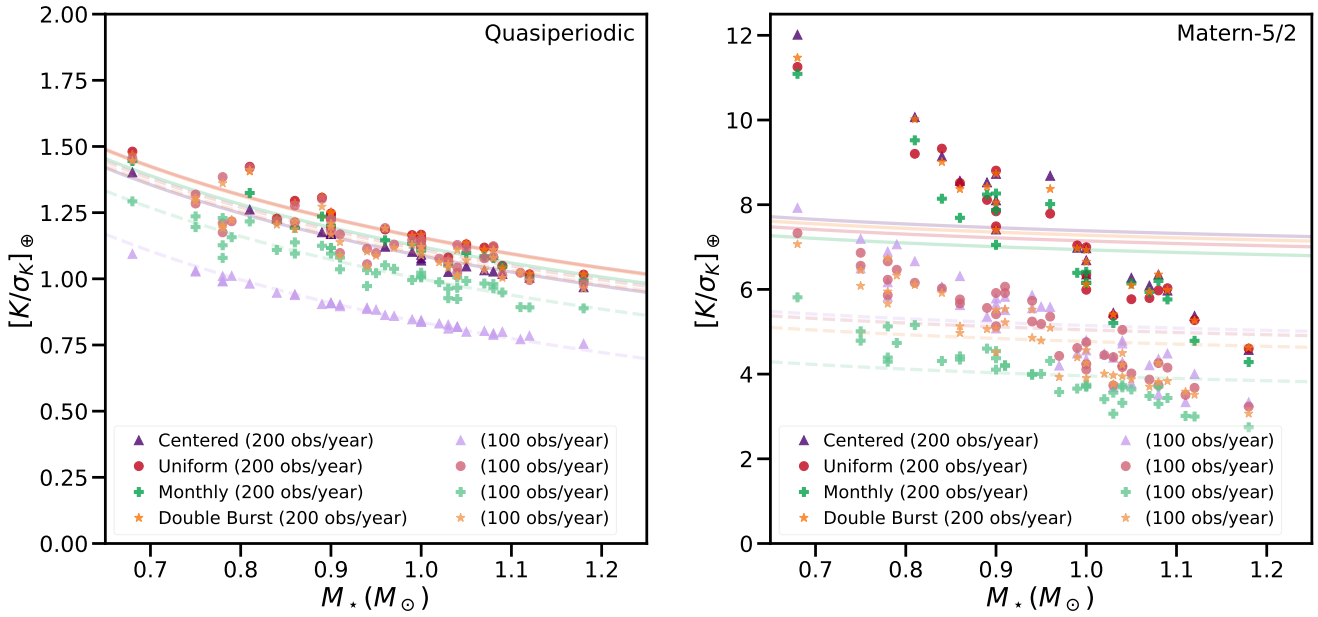


Figure 10. Dependence of expected Earth analog detection significance on stellar mass for each of our simulated surveys. On the left, we show that for the quasiperiodic kernel, $[K/\sigma_K]_\oplus$ follows a $K \propto M_\star^{-2/3}$ curve for every strategy. That is, σ_K is independent of stellar mass. On the right, we show that the $[K/\sigma_K]_\oplus$ has a much steeper dependence on $M_\star$, suggesting that σ_K depends on stellar mass as well.

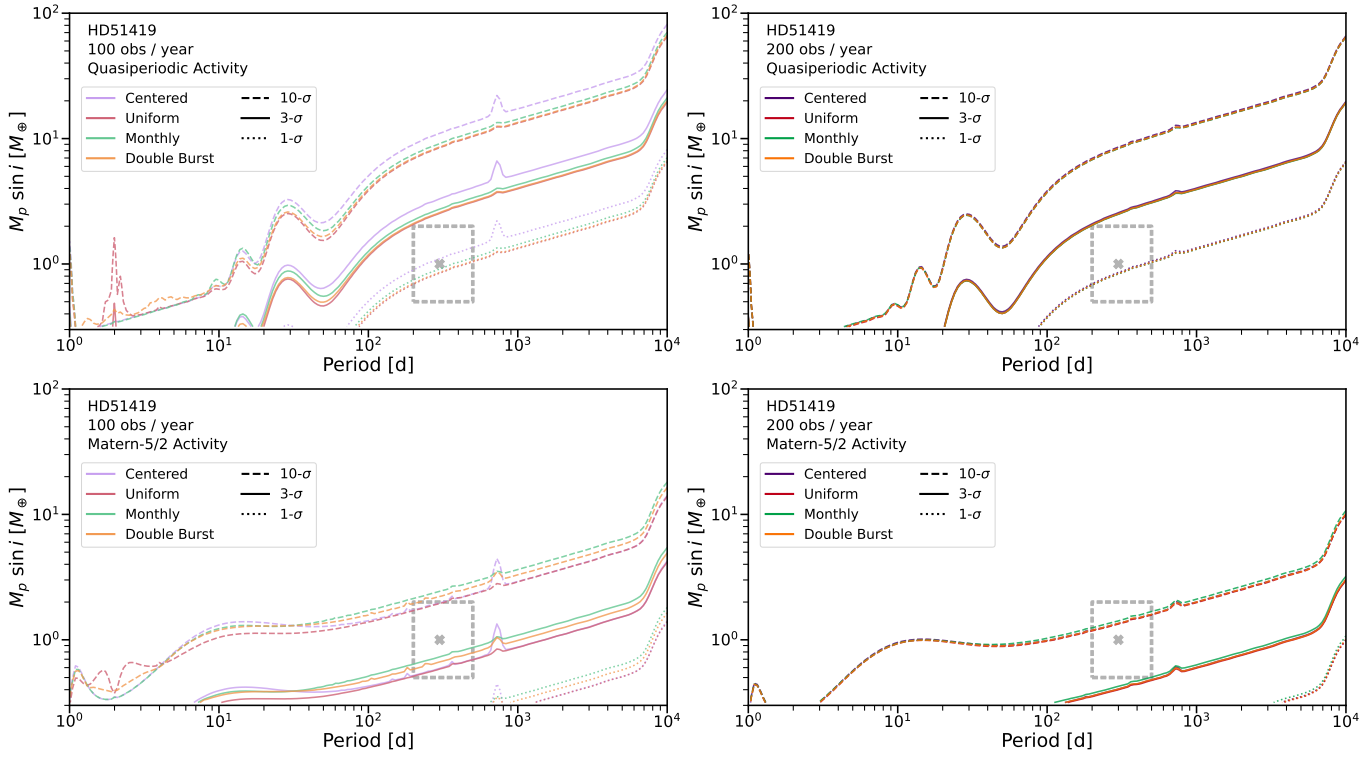


Figure 11. Detection significance contours for a typical target star. For each simulated survey, we show the $K/\sigma_K = 10$, 3, and 1 contours as solid, dotted, solid, and dashed lines, respectively. Certain features are more prominent for some survey strategies, such as the strong two-year alias peak for the Centered strategy and the lower sensitivity of the Uniform strategy to short-period planets. But at each significance level, it is clear that the local slope within the $D_\oplus$ Earth analog region (grey) does not change from strategy to strategy.

We describe the design and execution of several tests with which we isolate and assess the impact of sources of noise on different timescales. From our simulations of survey schedules with different intra-night visit distributions, we show that:

- distributed multi-visit strategies outperform single-visit strategies across all nightly time costs in the presence of granulation alone, but this advantage is reversed for oscillations
- in the oscillations-only case, one can achieve higher precision for visits shorter than $\lesssim 20$ minutes by sampling the oscillation signal with a sequence of consecutive exposures instead of averaging over the signal with a single continuous exposure
- in the presence of correlated noise from oscillations and granulation together, single-visit strategies are generally preferred
- when we account for photon noise, multi-visit strategies are more heavily penalized by the precision loss incurred by overhead costs

Analogous survey schedule simulations are used to test the performance of different distributions of observations across an observing season, and we find that:

- dense, high-cadence observing strategies are preferred when rotationally modulated stellar activity signals are best represented by a Matern-5/2 kernel with a relatively short correlation length
- sparser observing strategies that maximize the seasonal observing baseline are preferred when these same signals are represented by a quasiperiodic kernel with a correlation length on par with the Solar rotation period

These findings are applied to simulations of 10-year EPRV exoplanet surveys with realistic target lists and time constraints as well as practical observing constraints such as weather losses, intra-survey competition, and seasonal observability. We calculate and compare the expected Fisher information content for each survey and show that the results of these more comprehensive simulations are largely consistent with those of the isolated tests. We also quantify the absolute detection sensitivity limits we will expect to achieve and discuss our findings. For the Matern-5/2 activity kernel, we expect to be sensitive Earth analog exoplanets around as many as ~ 20 quiet stars at the $[K/\sigma_K]_\oplus > 5$ level for most survey strategies, whereas for the quasiperiodic kernel, we will achieve a typical detection significance of just $[K/\sigma_K]_\oplus > 1$.

We also summarize several caveats to our results, the most important of which is that our analysis implicitly assumes perfect knowledge of the GP kernels with which we represent each source of stellar variability. Our results show that the optimal survey strategy will depend strongly on the assumed hyperparameters and GP kernel form for certain sources of noise, suggesting that we should exercise caution in applying Fisher information analysis to specific stars for which these values are not well constrained. However if the kernels and hyperparameters are known to high accuracy and precision, the analysis framework we have outlined here can be a powerful tool with which we can identify more efficient and effective observing strategies both for individual stars as well as for an entire survey.

9. ACKNOWLEDGEMENTS

The authors would like to thank David W. Hogg for illuminating discussions on the application and interpretation of Fisher information analysis in this work, Jacob Luhn for his assistance with the oscillation and granulation GP kernel integrations, Christian Gilbertson for their guidance on the use of Cholesky factorization for matrix inversion and for discussions on the efficacy of different stellar activity kernels, and Sam Thompson and Annelies Mortier for feedback on historical weather patterns at La Palma. We also appreciate the support and feedback from NEID science team members including Jason Wright, Suvrath Mahadevan, and Eric Ford as well as from members of the Astronomical Data group at the Center for Computational Astrophysics as this project progressed.

The Pennsylvania State University campuses are located on the original homelands of the Erie, Haudenosaunee (Seneca, Cayuga, Onondaga, Oneida, Mohawk, and Tuscarora), Lenape (Delaware Nation, Delaware Tribe, Stockbridge-Munsee), Shawnee (Absentee, Eastern, and Oklahoma), Susquehannock, and Wahzhazhe (Osage) Nations. As a land grant institution, we acknowledge and honor the traditional caretakers of these lands and strive to understand and model their responsible stewardship. We also acknowledge the longer history of these lands and our place in that history. The Center for Exoplanets and Habitable Worlds is supported by the Pennsylvania State University and the Eberly College of Science. This research has made use of the SIMBAD database, operated at CDS, Strasbourg, France, and NASA's Astrophysics Data System Bibliographic Services.

Software: astroplan (Morris et al. 2018), astropy (Astropy Collaboration et al. 2018), matplotlib (Hunter 2007), numpy (Harris et al. 2020), scipy (Oliphant 2007)

REFERENCES

Aigrain, S., & Foreman-Mackey, D. 2022, arXiv e-prints, arXiv:2209.08940. https://arxiv.org/abs/2209.08940

Astropy Collaboration, Price-Whelan, A. M., Sipőcz, B. M., et al. 2018, AJ, 156, 123, doi: 10.3847/1538-3881/aabc4f

Baliunas, S. L., Hartmann, L., Noyes, R. W., et al. 1983, ApJ, 275, 752, doi: 10.1086/161572

Baum, A. C., Wright, J. T., Luhn, J. K., & Isaacson, H. 2022, AJ, 163, 183, doi: 10.3847/1538-3881/ac5683

Blackman, R. T., Fischer, D. A., Jurgenson, C. A., et al. 2020, AJ, 159, 238, doi: 10.3847/1538-3881/ab811d

Bonanno, A., Corsaro, E., & Karoff, C. 2014, A&A, 571, A35, doi: 10.1051/0004-6361/201424632

Bouchy, F., Díaz, R. F., Hébrard, G., et al. 2013, A&A, 549, A49, doi: 10.1051/0004-6361/201219979

Bouchy, F., Pepe, F., & Queloz, D. 2001, A&A, 374, 733, doi: 10.1051/0004-6361:20010730

Brewer, J. M., Fischer, D. A., Valenti, J. A., & Piskunov, N. 2016, ApJS, 225, 32, doi: 10.3847/0067-0049/225/2/32

Brewer, J. M., Fischer, D. A., Blackman, R. T., et al. 2020, AJ, 160, 67, doi: 10.3847/1538-3881/ab99c9

Bryan, M. L., Knutson, H. A., Lee, E. J., et al. 2019, AJ, 157, 52, doi: 10.3847/1538-3881/aaf57f

Cattaneo, F., Emonet, T., & Weiss, N. 2003, ApJ, 588, 1183, doi: 10.1086/374313

Chaplin, W. J., Cegla, H. M., Watson, C. A., Davies, G. R., & Ball, W. H. 2019, AJ, 157, 163, doi: 10.3847/1538-3881/ab0c01

Cloutier, R., Doyon, R., Bouchy, F., & Hébrard, G. 2018, AJ, 156, 82, doi: 10.3847/1538-3881/aacea9

Cosentino, R., Lovis, C., Pepe, F., et al. 2012, in Society of Photo-Optical Instrumentation Engineers (SPIE) Conference Series, Vol. 8446, Ground-based and Airborne Instrumentation for Astronomy IV, ed. I. S. McLean, S. K. Ramsay, & H. Takami, 84461V, doi: 10.1117/12.925738

Crass, J., Gaudi, B. S., Leifer, S., et al. 2021, arXiv e-prints, arXiv:2107.14291. https://arxiv.org/abs/2107.14291

Cumming, A. 2004, MNRAS, 354, 1165, doi: 10.1111/j.1365-2966.2004.08275.x

Dumusque, X., Udry, S., Lovis, C., Santos, N. C., & Monteiro, M. J. P. F. G. 2011, A&A, 525, A140, doi: 10.1051/0004-6361/201014097

Fang, J., & Margot, J.-L. 2012, ApJ, 761, 92, doi: 10.1088/0004-637X/761/2/92

Fisher, R. A. 1922, Philosophical Transactions of the Royal Society of London Series A, 222, 309, doi: 10.1098/rsta.1922.0009

García, R. A., Pérez Hernández, F., Benomar, O., et al. 2014, A&A, 563, A84, doi: 10.1051/0004-6361/201322823

Gilbertson, C., Ford, E. B., & Dumusque, X. 2020a, Research Notes of the American Astronomical Society, 4, 59, doi: 10.3847/2515-5172/ab8d44

Gilbertson, C., Ford, E. B., Jones, D. E., & Stenning, D. C. 2020b, ApJ, 905, 155, doi: 10.3847/1538-4357/abc627

Gomes, D. C. H., Murray, Z., Gomes, R. C. H., Holman, M. J., & Bernstein, G. M. 2022, arXiv e-prints, arXiv:2212.09594, doi: 10.48550/arXiv.2212.09594

Guo, Z., Ford, E. B., Stello, D., et al. 2022, arXiv e-prints, arXiv:2202.06094. https://arxiv.org/abs/2202.06094

Gupta, A. F., Wright, J. T., Robertson, P., et al. 2021, AJ, 161, 130, doi: 10.3847/1538-3881/abd79e

Gupta, A. F., Luhn, J., Wright, J. T., et al. 2022, AJ, 164, 254, doi: 10.3847/1538-3881/ac96f3

Hall, R. D., Thompson, S. J., Handley, W., & Queloz, D. 2018, MNRAS, 479, 2968, doi: 10.1093/mnras/sty1464

Halverson, S., Terrien, R., Mahadevan, S., et al. 2016, in Society of Photo-Optical Instrumentation Engineers (SPIE) Conference Series, Vol. 9908, Ground-based and Airborne Instrumentation for Astronomy VI, ed. C. J. Evans, L. Simard, & H. Takami, 99086P, doi: 10.1117/12.2232761

Harris, C. R., Millman, K. J., van der Walt, S. J., et al. 2020, Nature, 585, 357, doi: 10.1038/s41586-020-2649-2

Haywood, R. D., Milbourne, T. W., Saar, S. H., et al. 2022, ApJ, 935, 6, doi: 10.3847/1538-4357/ac7c12

Hojjatpanah, S., Figueira, P., Santos, N. C., et al. 2019, A&A, 629, A80, doi: 10.1051/0004-6361/201834729

Howard, A. W., & Fulton, B. J. 2016, PASP, 128, 114401, doi: 10.1088/1538-3873/128/969/114401

Howard, A. W., Marcy, G. W., Johnson, J. A., et al. 2010, Science, 330, 653, doi: 10.1126/science.1194854

Hunter, J. D. 2007, Computing in Science and Engineering, 9, 90, doi: 10.1109/MCSE.2007.55

Jiménez-Reyes, S. J., García, R. A., Jiménez, A., & Chaplin, W. J. 2003, ApJ, 595, 446, doi: 10.1086/377304

Jurgenson, C., Fischer, D., McCracken, T., et al. 2016, in Society of Photo-Optical Instrumentation Engineers (SPIE) Conference Series, Vol. 9908, Ground-based and Airborne Instrumentation for Astronomy VI, ed. C. J. Evans, L. Simard, & H. Takami, 99086T, doi: 10.1117/12.2233002

Kipping, D. M. 2013, MNRAS, 434, L51, doi: 10.1093/mnrasl/slt075

Laliotis, K., Burt, J. A., Mamajek, E. E., et al. 2023, arXiv e-prints, arXiv:2302.10310. https://arxiv.org/abs/2302.10310

Langellier, N., Milbourne, T. W., Phillips, D. F., et al. 2021, AJ, 161, 287, doi: 10.3847/1538-3881/abf1e0

Luhn, J. K., Ford, E. B., Guo, Z., et al. 2023, AJ, 165, 98, doi: 10.3847/1538-3881/acad08

Mathur, S., García, R. A., Bugnet, L., et al. 2019, Frontiers in Astronomy and Space Sciences, 6, 46, doi: 10.3389/fspas.2019.00046

Mayor, M., & Queloz, D. 1995, Nature, 378, 355, doi: 10.1038/378355a0

Mayor, M., Marmier, M., Lovis, C., et al. 2011, arXiv e-prints, arXiv:1109.2497. https://arxiv.org/abs/1109.2497

Morris, B. M., Tollerud, E., Sipőcz, B., et al. 2018, AJ, 155, 128, doi: 10.3847/1538-3881/aaa47e

Motalebi, F., Udry, S., Gillon, M., et al. 2015, A&A, 584, A72, doi: 10.1051/0004-6361/201526822

Newman, P. D., Plavchan, P., Burt, J. A., et al. 2022, arXiv e-prints, arXiv:2204.13968. https://arxiv.org/abs/2204.13968

Nicholson, B. A., & Aigrain, S. 2022, MNRAS, 515, 5251, doi: 10.1093/mnras/stac2097

Oliphant, T. E. 2007, Computing in Science and Engineering, 9, 10, doi: 10.1109/MCSE.2007.58

Pepe, F., Cristiani, S., Rebolo, R., et al. 2021, A&A, 645, A96, doi: 10.1051/0004-6361/202038306

Pereira, F., Campante, T. L., Cunha, M. S., et al. 2019, MNRAS, 489, 5764, doi: 10.1093/mnras/stz2405

Petersburg, R. R., Ong, J. M. J., Zhao, L. L., et al. 2020, AJ, 159, 187, doi: 10.3847/1538-3881/ab7e31

Rajpaul, V., Aigrain, S., Osborne, M. A., Reece, S., & Roberts, S. 2015, MNRAS, 452, 2269, doi: 10.1093/mnras/stv1428

Rosenthal, L. J., Fulton, B. J., Hirsch, L. A., et al. 2021, ApJS, 255, 8, doi: 10.3847/1538-4365/abe23c

Rosenthal, L. J., Knutson, H. A., Chachan, Y., et al. 2022, ApJS, 262, 1, doi: 10.3847/1538-4365/ac7230

Schwab, C., Rakich, A., Gong, Q., et al. 2016, in Society of Photo-Optical Instrumentation Engineers (SPIE) Conference Series, Vol. 9908, Ground-based and Airborne Instrumentation for Astronomy VI, ed. C. J. Evans, L. Simard, & H. Takami, 99087H, doi: 10.1117/12.2234411

Suárez Mascareño, A., Rebolo, R., González Hernández, J. I., & Esposito, M. 2015, MNRAS, 452, 2745, doi: 10.1093/mnras/stv1441

Sulis, S., Lendl, M., Cegla, H., et al. 2022, arXiv e-prints, arXiv:2211.14398, doi: 10.48550/arXiv.2211.14398

Tegmark, M., Taylor, A. N., & Heavens, A. F. 1997, ApJ, 480, 22, doi: 10.1086/303939

Thompson, S. J., Queloz, D., Baraffe, I., et al. 2016, in Society of Photo-Optical Instrumentation Engineers (SPIE) Conference Series, Vol. 9908, Ground-based and Airborne Instrumentation for Astronomy VI, ed. C. J. Evans, L. Simard, & H. Takami, 99086F, doi: 10.1117/12.2232111

Van Eylen, V., Albrecht, S., Huang, X., et al. 2019, AJ, 157, 61, doi: 10.3847/1538-3881/aaf22f

Zechmeister, M., Kürster, M., & Endl, M. 2009, A&A, 505, 859, doi: 10.1051/0004-6361/200912479

Zhao, L., Fischer, D. A., Ford, E. B., et al. 2020, Research Notes of the American Astronomical Society, 4, 156, doi: 10.3847/2515-5172/abb8d0

Zhao, L. L., Fischer, D. A., Ford, E. B., et al. 2022, AJ, 163, 171, doi: 10.3847/1538-3881/ac5176

Zhu, W. 2022, AJ, 164, 5, doi: 10.3847/1538-3881/ac6f59